

THE ENERGY DEPENDENCE OF π^+_p BACKWARD
ELASTIC SCATTERING FROM 2 TO 6 GeV/c

A Dissertation

Submitted to the Graduate School of the
University of Notre Dame in Partial Fulfillment
of the Requirements for the Degree of
Doctor of Philosophy

by

Sister Arlene Judith Lennox, SSJ, B. S., M. S.

Co-Director

Co-Director

Department of Physics

Notre Dame, Indiana

August, 1974

ABSTRACT

The data obtained in this experiment were used to systematically study the energy dependence of the 180° differential cross section for π^+p elastic scattering in the center-of-mass energy region from 2159 to 3490 MeV. Measurements were made for incident pion momenta between 2.0 and 6.0 in steps of typically 100 MeV/c. A focussing spectrometer and scintillation counter hodoscopes were used to obtain angular distributions for pions scattering in the angular range 141° to 173° in the laboratory. In general, these angular distributions exhibited an exponential u dependence, where u is the square of the four momentum transfer between the incident pion and the recoil proton. Hence, values for $d\sigma/d\Omega$ at 180° were found by making fits to the form $d\sigma/d\Omega = d\sigma/d\Omega(180^\circ) \exp[b(u - u_{\max})]$, where b is a slope parameter.

A resonance model and an interference model were used to perform fits to the energy dependence of $d\sigma/d\Omega(180^\circ)$. Both models led to equally good fits to the data and predicted values for the masses, widths, parities, and the product of spin and elasticity for the $\Delta(2200)$, $\Delta(2420)$, $\Delta(2850)$, and $\Delta(3230)$ resonances. On the basis of backward scattering alone it was not possible to determine which model more accurately describes pion-nucleon scattering. However, both models required the existence of a $\Delta(2200)$ in order to produce satisfactory fits to the data obtained in this experiment.

Fig. 19.	Energy dependence of the 180° differential cross section.	73
Fig. 20.	Schematic representation of the direct-channel and crossed-channel amplitudes.	77
Fig. 21.	Breit-Wigner curve for the $\Delta(2850)$.	80
Fig. 22.	Regge model fit to the data.	83
Fig. 23.	Imaginary part of the π^+p scattering amplitude.	90
Fig. 24.	Real part of the π^+p scattering amplitude.	92
Fig. 25.	Resonance model fit to the data.	97
Fig. 26.	Program JUDY flowchart.	103
Fig. 27.	Listing of RLEC.	105
Fig. 28.	Hodoscope correlation matrices.	108
Fig. 29.	Momentum dependence in the noncentral ϕ^B counters.	111
Fig. 30.	Angular distributions for the noncentral ϕ^B counters.	113

CHAPTER I

INTRODUCTION

In the center-of-mass energy region above 2100 MeV, where a large number of partial waves makes phase shift analyses difficult, it is possible to obtain information on the existence and properties of resonances by studying backward scattering. Because non-resonant diffractive scattering dominates forward scattering the structure associated with resonances is obscured in the total and forward cross sections. However, the presence of resonances produces distinct structure in the energy dependence of $d\sigma/d\Omega(180^\circ)$. Evidence for this structure has been seen in a number of π^+p backward elastic scattering experiments performed in the center of mass energy region from 2159 to 3490 MeV. Some of these experiments were done specifically to study scattering at 180° while others reported values close to 180° . Experiments listed in references [1] through [21] are those reporting differential cross sections in the region of the backward peak. This region corresponds to values of u greater than -0.14 (GeV/c)^2 , where $u = (P_\pi - P_p)^2$ and P_π and P_p are the four momenta of the incident pion and recoil proton, respectively. A plot of the values for backward or near backward cross sections available when this experiment was proposed is shown in Figure 1.

The purpose of this experiment was to systematically study the

Figure 1. The near backward elastic π^+p cross sections available when this experiment was proposed. The BNL-ROCHESTER [6] data and the CERN-SACLAY [2] data correspond to $\cos\theta = -1$. The point at 5.9 GeV/c was calculated for $\cos\theta = -1$ from a BNL-CORNELL [15] fit and is plotted without error bars. The remaining experimental points correspond to the following center-of-mass scattering angles: BNL-CORNELL-MICHIGAN [12], $\cos\theta = -0.996$; CERN [3], $\cos\theta = -0.987$; JINR [18] at 3.15, 4.10, and 4.85 GeV/c, $\cos\theta \approx -0.999$; other JINR [11] points, $\cos\theta \approx -0.994$.

energy dependence in $\pi^+ p$ backward elastic scattering in the region 2159 to 3490 MeV by taking data for incident pion momenta between 2.0 and 6.0 GeV/c in steps of typically 100 MeV/c. The experiment was performed at Argonne National Laboratory and was designated E-262. A focussing spectrometer and scintillation counter hodoscope distinguished the higher momentum of the forward going protons from the lower momentum of the beam particles. Scintillation counter hodoscopes detected the scattering angles of the forward protons and the backward pions. Angular distributions were obtained for pions scattering in the range 141° to 173° in the laboratory and the values for $d\sigma/d\Omega$ at 180° were found by extrapolation.

Two models were used to perform fits to the data. These resulted in values for the masses, widths, parities and the product of spin and elasticity for the $\Delta(2200)$, $\Delta(2420)$, $\Delta(2850)$, and $\Delta(3230)$ resonances. When the experiment was begun there was no established negative parity resonance at ~ 2200 MeV. This experiment has provided strong evidence for its existence and, in addition, has improved our knowledge of the parameters describing the $\Delta(2420)$, $\Delta(2850)$, and $\Delta(3230)$ resonances.

CHAPTER II

EXPERIMENTAL SETUP AND PROCEDURES

2.1 INTRODUCTION

The beam of pions required for the experiment was produced at the zero gradient synchrotron (ZGS) of Argonne National Laboratory. A layout of the apparatus used to obtain differential cross sections in the near backward direction is shown in Figure 2. The incident pions were identified by scintillation counters and two threshold Čerenkov counters. They interacted with protons in a liquid hydrogen target and the reaction products were detected by scintillation counter hodoscopes. Interactions of interest in this experiment involved the production of a backward pion which entered the backward θ^B, ϕ^B hodoscope and a forward proton which entered the forward θ^F, ϕ^F hodoscope and the focussing spectrometer. For incident pion momenta from 2 to 6 GeV/c, the recoil proton produced in a backward elastic scattering has momentum approximately 300 to 400 MeV/c greater than beam momentum. The spectrometer easily separated such protons from the beam particles and focussed them on the momentum hodoscope. A Čerenkov counter just downstream of the momentum hodoscope was used to veto events in which pions had entered the hodoscope as a result of scattering from an object such as the pole tip of the last spectrometer magnet.

Conventional logic circuitry identified events and measured

Figure 2. Experimental layout.

appropriate rates on scalars. Information on the specific combination of counters involved in each individual event was recorded in coincidence registers (latches). Finally, data from the scalars and latches were read into an on-line computer which monitored the experiment and recorded the data on magnetic tape.

The remainder of this chapter is devoted to reporting more detailed information on the apparatus itself and the procedures used to obtain the data.

2.2 EXPERIMENTAL LAYOUT

The incident pions were produced when a beam of protons extracted from the main ring of the ZGS impinged on a $10.2 \times .64 \times .64$ cm³ beryllium production target. Each beam spill lasted approximately 500 msec and was essentially structureless except for the periodic bunching caused by the 13.98 MHz radio frequency in the main ring. Figure 3 shows the quadrupole and bending magnets used to deliver the beam from the production target to the area where the experiment was performed. The beam's size and momentum dispersion, $\Delta P/P$, could be adjusted by changing the width of the momentum slit, labeled MS in the figure. The dispersion was such that 0.65 cm corresponded to 0.5% $\Delta P/P$. For most of the data taking the slit width was ~ 2.54 cm, producing a dispersion of $\pm 1\%$. The systematic error on the central value of the momentum of the beam was estimated to be $\pm 0.6\%$.

Figure 3. Layout of beam transport system.

Of the $\sim 2 \times 10^6$ secondary beam particles delivered per ZGS pulse approximately 60% were pions, 34% were protons, and the remaining 6% were positrons, muons and kaons.

The following counters were used to identify beam pions: scintillation counters B1, B2, B3, B4, AT1 and BV1, and Čerenkov counters C1, C2 and C4. Of these B1, B2, B3, C1 and C2 are shown in Figure 2 and C4 is shown in Figure 3. Counter B4 was centered on the beam line 96.5 cm upstream of the center of the hydrogen target while AT1, an inverted U - shaped veto counter, shadowed the top and sides of the target vacuum jacket. The beam-halo veto counter, BV1, was just upstream of the backward hodoscope, below B3. Counters B1 and B2 were circular with diameter 14 cm and B4 was circular with diameter 3.8 cm. B3 was 6.4 cm vertical by 7.6 cm horizontal. Čerenkov counters C1 and C2 were 15.2 cm in diameter and 100 cm long. They contained Freon-13 and operated at pressures ranging from 25 to 60 psig depending on the incident beam momentum. C4 was 10.2 cm in diameter and 100 cm long. It contained Freon-12 and its operating pressures ranged from 7.5 to 14.5 psia.

The hydrogen target shown in Figure 4 consisted of a flask surrounded by a vacuum jacket. The target flask was cylindrical, 5.1 cm in diameter by 25.4 cm in length, and contained liquid hydrogen at a vapor pressure of ~ 13 psia. Its walls were constructed from one

Figure 4. The liquid hydrogen target (a) cross section through the center plane of the target, (b) cross-section of the downstream end.

layer of mylar 0.013 cm thick covered with seven layers of super-insulating material. Each layer of superinsulating material was 0.0006 cm mylar coated with a layer of aluminum 200 \AA thick. The upper and side walls of the vacuum jacket were stainless steel while the bottom and both ends were 0.025 cm thick mylar. The mylar bottom was a necessary feature, permitting the recoil pions to freely enter the backward hodoscope.

The backward scattered pions were located in both azimuthal, ϕ^B , and polar, θ^B , angles by a scintillation counter hodoscope below the incident beam line. Six similar counters, each 22.9 cm wide, separated the pions into six angular bins of θ^B from about 173° to 141° in the laboratory. Five of these, designated θ_1^B through θ_5^B , were placed along the circumference of a circle of radius 137 cm with its center at the center of the hydrogen target as shown in Figure 2. They were arranged with θ_5^B closest to the beam and θ_1^B farthest away from it. The sixth counter, labeled \mathcal{D} , overlapped θ_5^B and θ_4^B so as to divide each of them into two smaller bins. Thus, the coincidences $\mathcal{D} \cdot \theta_5^B$ and $\mathcal{D} \cdot \theta_4^B$ along with $\bar{\mathcal{D}} \cdot \theta_5^B$ and $\bar{\mathcal{D}} \cdot \theta_4^B$ subtended polar angles half as large as those subtended by θ_3^B through θ_1^B . Because the $\bar{\mathcal{D}} \cdot \theta_5^B$ bin extended into the beam halo, the data in this bin were contaminated with beam accidentals and were not included in the analysis. Counters immediately upstream of the θ^B counters separated the recoil pions

into three bins of ϕ^B . The central counter, ϕ_C^B , covered the azimuthal angular range $\pm 5.4^\circ$ from the backward direction; ϕ_{nc}^{B1} extended the range to $+10.9^\circ$ and ϕ_{nc}^{B2} extended it to -10.9° . A counter, $T\pi$, located between the hydrogen target and the backward hodoscope indicated that a pion entering the backward hodoscope had originated in the target region.

The forward going recoil protons were located in azimuth by a counter, ϕ^F , which was mounted on the upstream end of the first quadrupole magnet in the spectrometer. This counter was narrow (1.4 cm) and limited the data to scatterings which took place in a nearly vertical plane defined by the trajectories of the incoming pion and the recoil proton. The polar scattering angle, θ^F , was divided into seven bins by counters mounted just downstream of ϕ^F . The vertical distance covered by the θ^F hodoscope was 21.1 cm, with the bottom of the lowest counter placed 2.6 cm above the beam center line.

The focussing spectrometer separated the forward going recoil protons from the beam particles and from other scattered particles whose momentum was close to the beam momentum. It consisted of two QM102 quadrupole magnets and a BM109 dipole magnet, with the optical axis pitched vertically to increase the polar angular acceptance. The first quadrupole downstream of the hydrogen target was horizontally defocussing and the second was horizontally focussing. This choice of optics produced an image of the target which was magnified vertically

and reduced horizontally. The dipole magnet, which was located between the two quadrupoles, deflected beam particles 9° horizontally from the nominal beam line. Because of the limited bending power of the magnet the spectrometer length was increased for beam momenta greater than 4.6 GeV/c. This was accomplished by moving the target, C-magnet, and backward hodoscope upstream, adjusting the angular orientation of the three spectrometer magnets to obtain a smaller pitch angle, and moving the momentum hodoscope downstream. Data was taken at 4.4 GeV/c and 4.6 GeV/c for both spectrometer lengths so that consistency checks could be made for the two geometries. For taking data at momenta from 2.0 to 4.6 GeV/c the face of the first spectrometer quadrupole was 205 cm from the hydrogen target and the θ^F hodoscope mounted on its face accepted protons at polar angles up to 6.6° from the beam line. For momenta from 4.4 to 6.0 GeV/c this distance was increased to 322.6 cm and protons were accepted at angles up to 4.2° . Other parameters describing the two spectrometer geometries are presented in Table I.

Transmissivity measurements and fine tuning adjustments for the spectrometer were made with the aid of a vertically deflecting dipole C-magnet surrounding the hydrogen target. This magnet was used only for adjusting or studying the parameters of the spectrometer and was turned off during normal data taking. One important adjustment which was made for each beam momentum involved focussing the

beam so that beam-momentum particles would not enter the momentum hodoscope. This was done by tuning the spectrometer bending magnet in the following manner. The C-magnet was used to vertically deflect the beam so as to align it along the spectrometer axis and then the current in the bending magnet was adjusted to position the beam on $P\pi$, a 2.54 cm wide scintillation counter located at the beam left side of the momentum hodoscope. The value of the bending magnet current obtained in this fashion was then used for normal data taking with the C-magnet turned off and insured the best possible separation of the recoil protons from the beam particles at the momentum hodoscope.

The C-magnet was also used to sweep the beam vertically across the θ^F hodoscope for transmissivity studies. During these studies the spectrometer magnets were set to correspond to a momentum on the order of 350 MeV/c lower than the incident beam momentum and the beam was systematically aimed at each of the θ^F counters. Thus, during the testing all the beam particles behaved like recoil protons with momenta higher than the beam momentum. Figure 5 shows a transmissivity curve for beam pions at 2.4 GeV/c with the spectrometer set for 2.0 GeV/c beam pions. In general the maximum spectrometer transmissivities ranged from 90% at the lower momenta to 100% at the higher momenta.

Figure 5. Transmissivity curve. The measurements were made using 2.4 GeV/c beam pions with Q7 and Q8 set to focus a 2.2 GeV/c beam and MB4 set to deflect a 2.0 GeV/c beam. The C-magnet (MB3) was used to sweep the beam across the spectrometer face and transmissivity was obtained as a function of the current in the C-magnet. The abscissa presented here has been converted from current to θ^F bins.

The recoil proton momentum hodoscope, P-HOD, was located at the spectrometer image plane on the high momentum side of $P\pi$. It contained twelve vertical scintillation counters, P_i^F , of 0.64 cm width in front of one vertical counter, PFF, 7.7 cm wide. The PFF, $P\pi$, and P_i^F counters were each 27.3 cm in height. A Čerenkov counter, C3, located just behind the momentum hodoscope was used to discriminate against pions in the hodoscope. This Čerenkov counter was 91 cm long and 30.5 cm in diameter. It contained Freon-12 and operated at pressures ranging from 25 to 40 psig.

2.3 LOGIC CIRCUITRY

The major elements of the logic circuitry used to identify good events and record appropriate information in scalers and latches are shown in Figures 6 to 9. The logic used to identify a beam pion is diagrammed in Figure 6. A prompt pion was identified by the coincidence $B1 \cdot B2 \cdot B3 \cdot B4 \cdot C1 \cdot C2 \cdot \overline{(AT1 + C4 + BV1)}$, defined as $B\pi$. Accidental rates in $B\pi$ were measured using the signal $B\pi A$, which had the same definition as $B\pi$ except for a 70 nsec delay in the $B1 \cdot B2 \cdot B3 \cdot B4$ signal.

The signal, PF, indicating that a beam pion had entered the hydrogen target and that a proton from the target had passed through the spectrometer and momentum hodoscope was defined by $PF = B\pi \cdot \overline{PFF \cdot \phi^F \cdot (C3 + P\pi)}$. The additional requirement that a pion had left

Figure 6. Beam pion identification logic. The $B\pi$ signal whose formation is shown here provided evidence that a pion had entered the target. It was required in the trigger.

Figure 7. Logic for identifying forward protons and backward pions. The πB signal whose formation is shown here provided evidence that a pion had entered the target and that a forward proton and backward pion had left the target. It was required in the trigger.

Figure 8. Formation of the θ^B signals entering the θ^B fan-in shown in Figure 7.

Figure 9. Formation of the event strobe signals.

the target and entered the backward hodoscope generated the signal, πB , defined by $\pi B = PF \cdot (\geq 10^B) \cdot T\pi \cdot \overline{BV1}$. Figure 7 shows the formation of PF and πB as well as the corresponding delayed signals PFA and πBA . Details of the formation of the θ^B signals are given in Figure 8.

A coincidence between πB and a signal from one of the counters in the backward ϕ hodoscope generated an event signal which strobed the latches and initiated the transfer of the data to the computer. The event signals $\pi BE = \phi_c^B \cdot \pi B$ and $\pi BB = \phi_{nc}^B \cdot \pi B$ distinguished between events where the backward pion entered the central ϕ^B counter and those where it entered one of the outer ϕ^B counters. The delayed πBE strobe, designated πBEA , was used to measure accidental rates. Signals from the θ^F and P^F hodoscopes were recorded in latches and read into the computer, but they were not required in the event strobe. Figure 9 shows the final stages of the logic circuitry used to generate the event signals.

2.4 ON-LINE COMPUTER

The experiment was monitored by a Varian 620i computer which was interfaced to the LeCroy latches and scalars. The on-line program performed its various jobs in the order of their assigned priorities. Highest priority was assigned to reading in the data, performing consistency checks on the data, and, finally, recording it on magnetic tape. Jobs in the next priority category were normally performed automatically but could be deleted by means of a sense

switch. They included printing the latch information for each event, printing error messages, and testing the values of the current in each of the magnets downstream of the production target. The latter job involved the use of a specially constructed interface which enabled the computer to automatically read the magnet currents and compare their values with a predetermined set of values. An error message immediately notified the experimenter when a current drifted outside the allowed limits. Lowest priority jobs were initiated only by a request from the operator via the teletype. These included a printing or scope display of the scalers or of the ratios of pairs of specified scalers as well as the request to end the run. In general, the execution of jobs in this category was interrupted whenever there was data waiting to be processed. Further details of the on-line program and the specific subroutine used to read the scalers and latches can be found in Appendix I.

2.5 SURVEY TECHNIQUES

Coordinates locating the scintillation counters relative to the center of the hydrogen target were obtained with the aid of two theodolites and an interactive survey program, SURVEY, which ran on the Varian 620i minicomputer. A designated point was viewed by each of the two theodolites, whose positions were known relative to the benchmarks laid down by standard surveying procedures. The polar and

azimuthal angular information from each theodolite was immediately entered into the computer and the program used a method of triangulation to find the midpoint of the shortest segment connecting the two lines of sight. This midpoint was taken to be the position of the designated point while the length of the segment provided an estimate of the error in the readings. Because this information was available within minutes after the measurement had been made it was possible to immediately identify and correct errors in measurement or transcription. The program also stored the coordinates of each point and could print out the location of any point relative to any other point. The use of this on-line survey method produced measurements with a precision of ± 0.01 cm for distances of 3 meters or less between the theodolite and the survey point and eliminated the problem of validating and correcting measurements after the first survey was completed.

CHAPTER III

DATA REDUCTION

3.1 INTRODUCTION

Data recorded on magnetic tape for each run included two types of information. The first was the total number of counts occurring in each scaler during the entire run. The second was the latch information, which could be decoded to ascertain the particular combination of counters involved in each individual event. During the data taking period the scaler information was particularly useful because it enabled the experimenter to quickly identify malfunctioning equipment. However, the correlation information obtained by decoding the latches proved to be invaluable in the off-line data reduction, particularly in estimating the background and in making appropriate cuts. It was the latched data rather than the data from the scalars that was finally used to calculate a differential cross section for each angular bin.

Two different methods of binning were used to study the u dependence of the differential cross sections. In the first method the data were organized into bins corresponding to each of the θ^B counters; in the second the bins corresponded to the θ^F counters. Both methods produced differential cross sections as a function of u , but each method involved an independent determination of the u values at which the cross sections were calculated. In general, the angular distributions thus obtained exhibited an exponential u dependence. Hence,

fits were made to the form $d\sigma/du = a \exp [b (u - u_{\max})]$ where a is the value of $d\sigma/du$ at 180° (the intercept) and b is the slope parameter.

Two fits were made for data taken at each of the thirty-eight incident pion momenta, one for the θ^B binning and the second for the θ^F binning.

For the remainder of this paper the first set of fits will be referred to as the " θ^B analysis" and the second as the " θ^F analysis."

3.2 HODOSCOPE CORRELATION MATRICES

The first stage of the data reduction process consisted of organizing the latch information into sets of matrices showing correlations among the θ^B , θ^F , and P^F counters. For each value of incident pion momenta two sets of matrices were generated, one set corresponding to data taken with a full target and the other set for empty target data. In each set the matrix element, M_{ij}^k , was the number of events which had triggered the k -th θ^B counter, the i -th P^F counter, and the j -th θ^F counter. The empty target subtraction was made by subtracting the appropriately normalized "empty" matrices from the "full" matrices. Visual inspection of the resulting matrices revealed a clear distinction between signal and background. In each matrix the signal was essentially confined to three or four of the θ^F bins between θ_1^F and θ_5^F , inclusive. Cuts on the θ^F counters were made by visually scanning the matrices and eliminating the θ^F bins which contained only background counts. The number of counts in θ_6^F and θ_7^F was always small and the contributions from these two counters were

not included in the final analysis. Application of the θ^F cuts reduced the raw data sample by an amount which varied from 2% to 20%.

The number of counts in a given θ^F bin excluded by the cuts was considered to be an estimate of the inelastic background for that particular θ^F counter. At a given momentum the background rate (background/number of beam pions) was found to be essentially constant as a function of θ^F and θ^B . However, the background rate per θ^F bin per θ^B bin did change smoothly with momentum, ranging from 9×10^{-10} at 2.0 GeV/c to 2×10^{-10} at 6.0 GeV/c. This rate is plotted as a function of momentum in Figure 10.

The correlation between the θ^B and θ^F counters for an incident pion momentum of 2.8 GeV/c is shown in Figure 11, which was obtained from the matrices by summing over the P^F counters, that is, by assuming over the index, i . The figure shows the data before the θ^F cuts and background subtraction were applied, but after the empty target subtraction had been made. Similar correlations were observed at all the other incident pion momenta.

By treating the data used to generate Figure 11 in a slightly different manner it is possible to illustrate the efficiency with which the spectrometer focussed the recoil protons. Figure 12 shows the momentum distribution of $\sim 12,000$ recoil protons at the momentum hodoscope. These protons were separated from a total of $\sim 1.1 \times 10^{10}$ positive beam pions which also entered the spectrometer. The

Figure 10. Background rate per θ^F bin per θ^B bin per 10^9 beam pions.

Figure 11. Correlation between θ^B and θ^F counters for 2.8 GeV/c beam pions. The figure shows the data after the empty target subtraction has been made, but before any other cuts or corrections have been applied.

Figure 12. Momentum distribution at the momentum hodoscope for $\sim 12,000$ recoil protons which were separated from $\sim 1.1 \times 10^{10}$ positive beam pions. The dashed curve represents that subset of recoil protons whose backward pions entered the beam-right ϕ_{nc}^{B2} counter and the dot-dashed curve indicates the number of recoil protons whose backward pions entered the beam-left ϕ_{nc}^{B1} counter. The data sample is the same as that used in Figure 11.

histogram was obtained by summing over the θ^F and θ^B counters, that is, by summing over the matrix indices k and j for an incident pion momentum of 2.8 GeV/c. Most of the signal was focussed on P^F counters 3, 4, and 5 while a considerable fraction of the signal in the wings was due to spatial and angular divergences in the beam rather than an aberration of the spectrometer. As is indicated in the figure, events in which the backward pion entered the beam-left ϕ_{nc}^{B1} counter tended to have recoil protons which entered the high momentum side of the hodoscope while counts in the beam-right ϕ_{nc}^{B2} counter tended to be correlated with the low momentum side of the hodoscope. These correlations were not unexpected in view of the spatial and angular divergences known to be present in the beam. A more detailed discussion of the matrices and the information obtained from them is given in Appendix II.

3.3 MONTE CARLO PROGRAMS

Geometric efficiencies were calculated in a Monte Carlo program which generated approximately 500,000 random events at each momentum. In this program the beam was assumed to have a Gaussian momentum distribution while its angular divergence and spatial distribution were constructed to be consistent with values actually measured for these quantities. The u distribution was chosen to reflect the approximate distribution of u values seen experimentally so that the Monte Carlo results would better represent the data, both systematically and

statistically. The program generated an event by choosing a beam particle, an interaction point in the target, and a value for momentum transfer, u . Straightforward kinematic and geometric calculations were then done to determine which θ^F and θ^B counters (if any) should detect the forward proton and backward pion. At each momentum an appropriate u range was chosen and divided into fifty bins. The geometric efficiency of each θ^F and θ^B counter was then calculated for each u bin. This resulted in two sets of geometric efficiencies for each momentum, one for the θ^B analysis and one for the θ^F analysis.

The spatial distribution and angular divergences of the beam used as input to the Monte Carlo were based on beam profiles measured using a pair of scintillation counters, photographic film, and a Segmented Wire Ion Chamber (SWIC). At the beginning of each run a Polaroid film was placed at the spectrometer entrance and exposed to the beam. The resulting pictures provided a continuous monitor of the shape and position of the beam at each incident pion momentum. More detailed studies of the beam were made using two 3 mm wide scintillation counters to scan the beam at positions 2.54 m upstream and downstream from the hydrogen target. Vertical profiles were obtained at both positions and a horizontal profile was measured at the upstream position. These profiles are shown in Figures 13 to 15. A downstream horizontal profile was obtained using the photographic film information in conjunction with the vertical profile at that

Figure 13. Upstream vertical beam profile measured 2.54 m from the hydrogen target for 4.7 GeV/c beam pions.

Figure 14. Downstream vertical beam profile measured 2.54 m from the hydrogen target for 4.7 GeV/c beam pions.

Figure 15. Upstream horizontal beam profile measured 2.54 m from the hydrogen target for 4.4 GeV/c beam pions at the high momentum spectrometer geometry.

position. The four profiles, the results of vertical position correlation studies, and computer studies based on the beam design program, TRANSPORT²², were used to determine the beam's effective focal point, ZF. The determination of ZF was made more precise by adjusting its value in the Monte Carlo program until the Monte Carlo prediction for the distribution of backward pions in the ϕ_c^B and ϕ_{nc}^B counters agreed with that observed experimentally. In a similar fashion, the precision in the determination of the beam height was improved by requiring that the slopes in the θ^F and θ^B analyses agree within statistical error. Both adjustments were within the experimental errors. Thus, the requirement of consistency between the θ^F and θ^B analyses as well as the requirement that the Monte Carlo correctly predict the backward ϕ distribution improved the reliability and accuracy of the Monte Carlo program used to generate geometric efficiencies.

Spectrometer transmissivities were calculated in a second Monte Carlo program, TURTLE²³. The shape of the calculated transmissivity as a function of θ^F agreed with the measured transmissivity shown in Figure 5. The previously mentioned (Section 3.2) lack of events in counters θ_6^F and θ_7^F was also consistent with the predictions of this program. Considering only the five θ^F counters used in the analysis, the transmissivities for momenta from 4.6 GeV/c to 6.0 GeV/c were all 100% and for 2.0 GeV/c to 4.6 GeV/c they were a

smooth function of θ^F , ranging from 87 to 99%. A tabulation of the transmissivities as a function of θ^F counters for each momentum is given in Table II.

3.4 CORRECTIONS TO THE DATA

The largest single correction to the data was necessitated by a defective optical coupling in a section of the ϕ^B hodoscope shadowing part of θ_1^B , θ_2^B , and θ_3^B . The fact that the ϕ^B hodoscope was included in the trigger requirement caused the loss of good events whose backward pion entered the inefficient part of the hodoscope. Due to the nature of the logic circuitry this inefficiency in the ϕ^B hodoscope caused an apparent inefficiency in the three θ^B counters. The corrections were, in fact, applied to the three θ^B bins as though those three counters had been inefficient. For θ_1^B and θ_2^B the efficiency was estimated to be $\sim 40\% \pm 7\%$ and for θ_3^B it was $\sim 55\% \pm 5\%$. The values obtained for the slopes of the angular distributions were sensitive to this correction and the error bars on the slopes are dominated by the errors associated with this correction. On the other hand, the values for the intercepts were essentially unaffected by the correction. Details of the methods used to estimate the efficiencies are included in Appendix II.

Additional corrections included the following: proton absorption in the target, 2%; pion absorption in the target before interaction, 1.5%; inefficiencies in the θ^F counters, 3.5%; and multiple counts in the θ^B

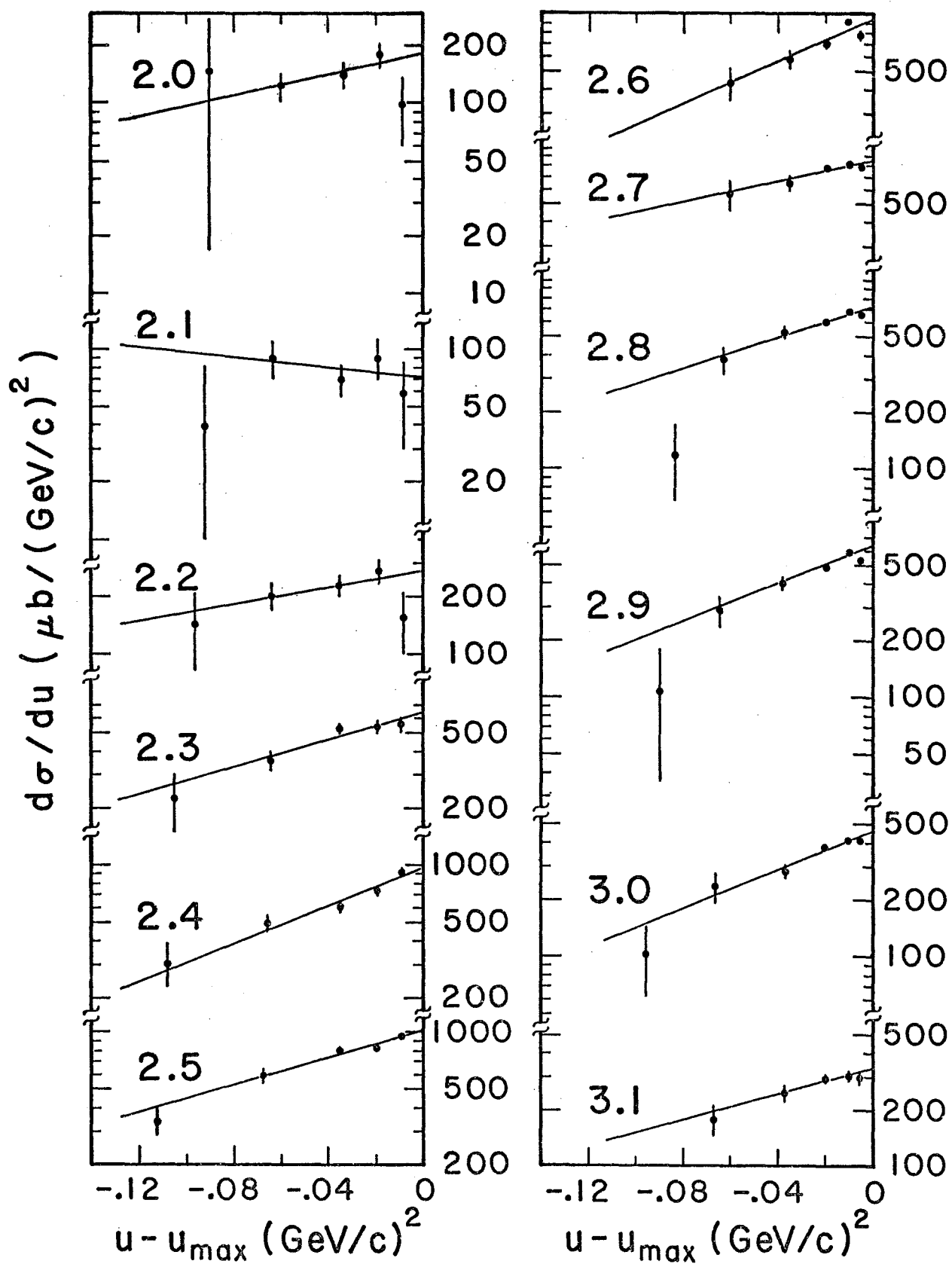
hodoscope, 4%. Pion absorption in the target after an interaction was u dependent, ranging from 4.6% for the $D\theta_5^B$ bin to 1.3% for the θ_1^B bin. An additional 1% correction was applied to the $D\theta_5^B$ bin for decay of the backward pion. The correction for accidental vetoes by the $P\pi$ and C3 counters was beam-rate dependent and ranged from 2% to 11%. Losses due to $B\pi$ pile-up were also rate dependent and ranged from 1% to 4%. Other possible sources of losses which were considered and found to be negligible include multiple Coulomb scattering, accidental events, beam accidentals, and dead times in the θ^B , ϕ^B , ϕ^F , and PFF counters.

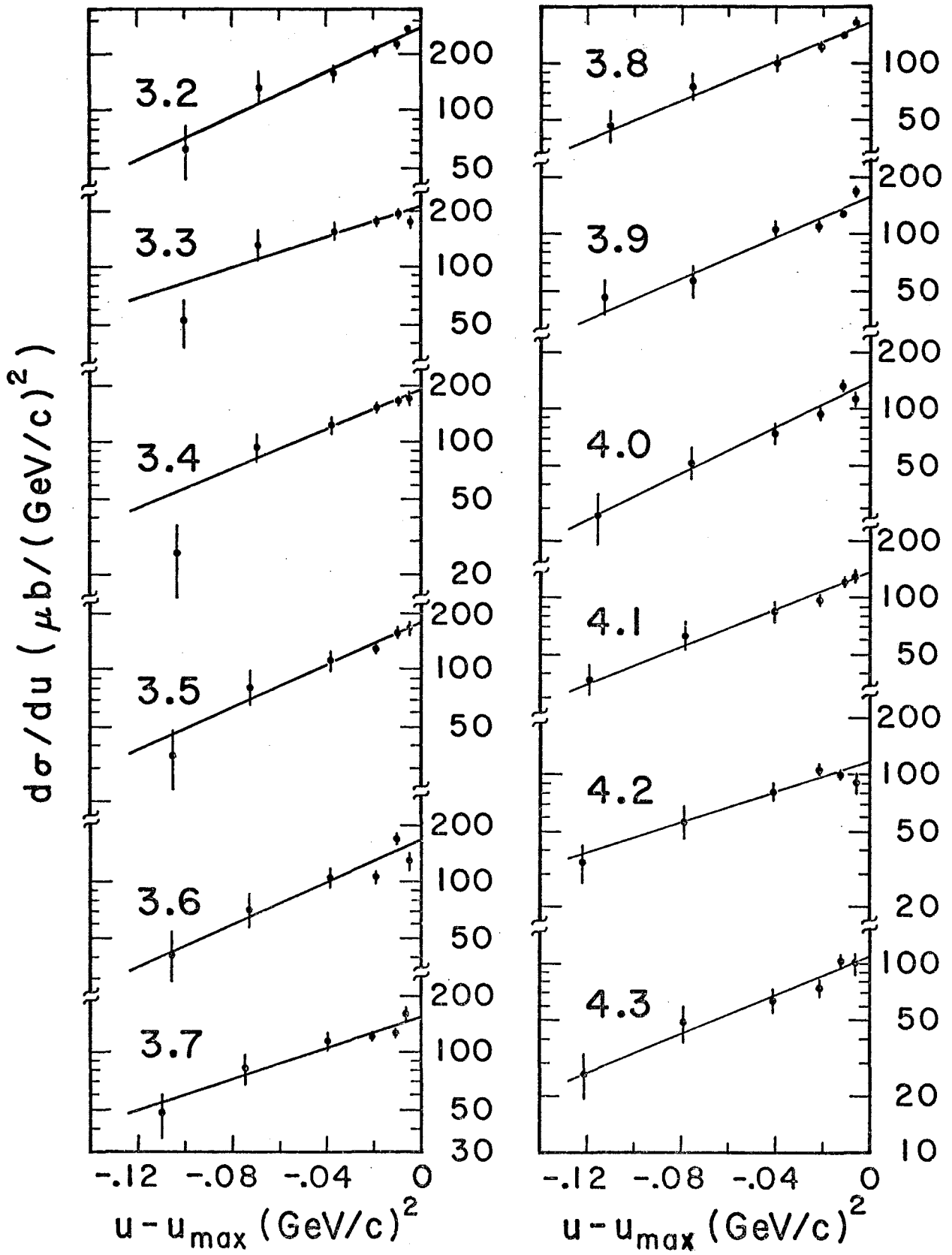
3.5 DETERMINATION OF SLOPES AND INTERCEPTS

The aforementioned correction factors and the efficiencies calculated in the two Monte Carlo programs were applied to the data in a fitting program called BAKFIT. For each value of incident pion momentum this program generated the angular distributions by calculating the appropriately weighted mean value of u corresponding to each hodoscope counter and converting the data from each counter to a differential cross section. It then found fits to the form $d\sigma/du = a \exp [b(u-u_{\max})]$ and calculated the best values and the associated errors for the slopes and intercepts. The angular distributions obtained in the θ^B analysis are listed in Table III and plotted in Figure 16. The straight lines shown in Figure 16 are the fits generated by BAKFIT. Table IV lists

Figure 16. Angular distributions obtained in the θ^B analysis.

The straight line fits were generated in program BAKFIT.





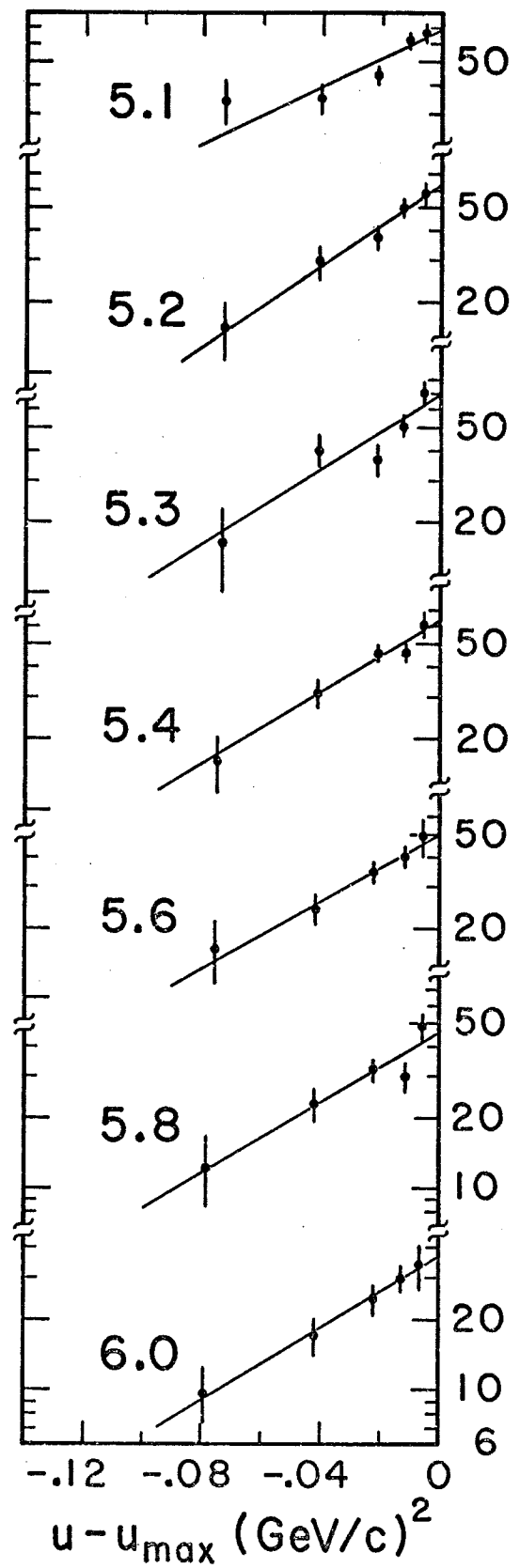
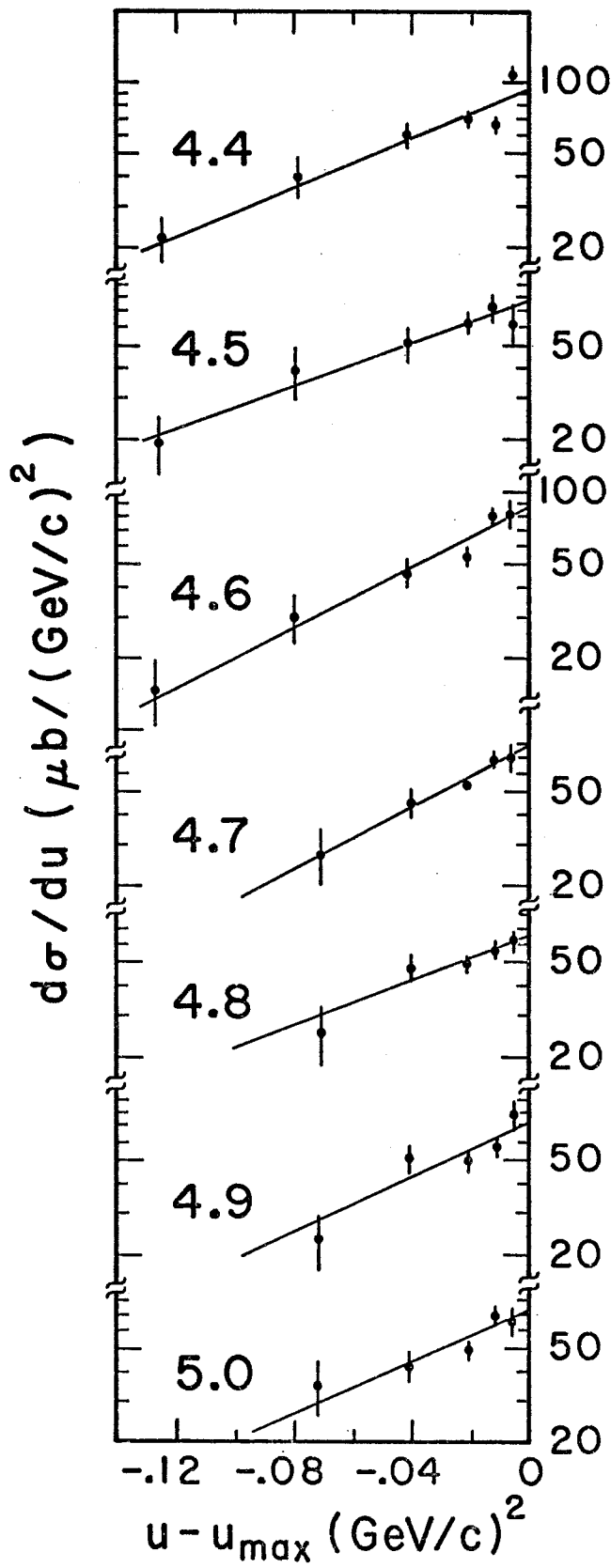


TABLE III. Angular distributions for the θ^B analysis.

u (GeV/c) ²	$d\sigma/du$ $\mu\text{b}/(\text{GeV}/c)^2$	$d\sigma/d\Omega$ $\mu\text{b}/\text{sr}$	$-\cos \theta_{c.m.}$	u (GeV/c) ²	$d\sigma/du$ $\mu\text{b}/(\text{GeV}/c)^2$	$d\sigma/d\Omega$ $\mu\text{b}/\text{sr}$	$-\cos \theta_{c.m.}$
2.0 GeV/c				2.8 GeV/c			
0.155	99.5 ± 40.5	23.9 ± 9.7	0.9984	0.115	667.8 ± 16.8	238.1 ± 6.0	0.9972
0.150	184.5 ± 28.0	44.4 ± 6.7	0.9965	0.110	688.6 ± 14.1	245.6 ± 5.0	0.9940
0.142	142.7 ± 22.7	34.3 ± 5.5	0.9937	0.101	606.5 ± 13.6	216.3 ± 4.8	0.9892
0.129	124.1 ± 23.0	29.8 ± 5.5	0.9888	0.083	537.0 ± 49.7	191.5 ± 17.7	0.9792
0.114	147.5 ± 130.1	35.5 ± 31.3	0.9830	0.058	387.5 ± 69.1	138.2 ± 24.6	0.9649
				0.038	122.2 ± 53.3	43.6 ± 19.0	0.9537
2.1 GeV/c				2.9 GeV/c			
0.149	59.0 ± 28.9	14.5 ± 7.1	0.9984	0.112	534.8 ± 26.1	198.5 ± 9.7	0.9970
0.143	91.5 ± 22.3	22.5 ± 5.5	0.9962	0.106	593.6 ± 23.8	220.3 ± 8.8	0.9936
0.136	70.1 ± 14.8	17.2 ± 3.6	0.9931	0.097	486.1 ± 21.8	180.4 ± 8.1	0.9887
0.121	92.0 ± 20.2	22.6 ± 5.0	0.9873	0.079	406.0 ± 41.6	150.7 ± 15.4	0.9782
0.107	39.9 ± 44.8	9.8 ± 11.0	0.9815	0.053	292.5 ± 55.5	108.6 ± 20.6	0.9626
				0.028	109.4 ± 73.4	40.6 ± 27.2	0.9485
2.2 GeV/c				3.0 GeV/c			
0.143	158.2 ± 57.2	42.6 ± 15.4	0.9982	0.108	413.4 ± 26.2	159.5 ± 10.1	0.9968
0.137	275.7 ± 41.6	74.2 ± 11.2	0.9959	0.102	411.6 ± 21.0	158.8 ± 8.1	0.9934
0.130	232.6 ± 34.6	62.6 ± 9.3	0.9926	0.094	382.9 ± 20.8	147.8 ± 8.0	0.9883
0.115	204.9 ± 35.7	55.2 ± 9.6	0.9864	0.076	284.2 ± 30.4	109.7 ± 11.7	0.9776
0.098	145.6 ± 64.1	39.2 ± 17.3	0.9794	0.047	234.1 ± 46.1	90.3 ± 17.8	0.9599
				0.018	103.1 ± 42.5	39.8 ± 16.4	0.9424
2.3 GeV/c				3.1 GeV/c			
0.137	559.5 ± 54.8	158.8 ± 15.6	0.9980	0.105	297.9 ± 26.7	119.3 ± 10.7	0.9968
0.132	539.2 ± 43.5	153.0 ± 12.3	0.9956	0.099	307.8 ± 20.5	123.3 ± 8.2	0.9932
0.124	524.0 ± 38.5	148.7 ± 10.9	0.9921	0.091	298.1 ± 18.3	119.4 ± 7.3	0.9880
0.109	354.6 ± 42.5	100.6 ± 12.1	0.9855	0.073	250.0 ± 28.0	100.1 ± 11.2	0.9766
0.089	228.3 ± 77.9	64.8 ± 22.1	0.9766	0.043	186.0 ± 36.7	74.5 ± 14.7	0.9575
2.4 GeV/c				3.2 GeV/c			
0.133	935.3 ± 52.1	279.0 ± 15.5	0.9979	0.102	274.6 ± 20.1	114.0 ± 8.3	0.9967
0.127	732.7 ± 47.8	218.6 ± 14.3	0.9954	0.096	230.7 ± 15.1	95.8 ± 6.3	0.9930
0.119	611.7 ± 47.8	182.5 ± 14.3	0.9918	0.088	210.5 ± 14.3	87.4 ± 5.9	0.9875
0.104	495.6 ± 55.3	147.8 ± 16.5	0.9846	0.070	162.5 ± 18.9	67.5 ± 7.8	0.9758
0.083	306.6 ± 77.9	91.5 ± 23.2	0.9747	0.039	138.6 ± 27.6	57.5 ± 11.5	0.9555
				0.007	66.0 ± 21.7	27.4 ± 9.0	0.9348
2.5 GeV/c				3.3 GeV/c			
0.128	964.9 ± 48.0	301.9 ± 15.0	0.9978	0.099	178.1 ± 19.3	76.6 ± 8.3	0.9965
0.122	821.0 ± 37.5	256.9 ± 11.7	0.9951	0.093	195.5 ± 13.0	84.0 ± 5.6	0.9926
0.115	809.0 ± 41.7	253.1 ± 13.0	0.9912	0.085	178.6 ± 12.0	76.8 ± 5.2	0.9869
0.099	596.1 ± 61.2	186.5 ± 19.1	0.9834	0.067	161.7 ± 17.9	69.5 ± 7.7	0.9746
0.076	336.2 ± 68.2	105.2 ± 21.3	0.9723	0.035	135.5 ± 26.2	58.2 ± 11.3	0.9529
				0.002	53.0 ± 15.2	22.8 ± 6.5	0.9310
2.6 GeV/c				3.4 GeV/c			
0.123	789.5 ± 57.1	258.5 ± 18.7	0.9975	0.096	174.2 ± 16.3	77.4 ± 7.2	0.9962
0.118	938.1 ± 52.0	307.1 ± 17.0	0.9947	0.091	168.4 ± 10.9	74.9 ± 4.8	0.9922
0.110	716.9 ± 45.9	234.7 ± 15.0	0.9906	0.082	153.1 ± 11.1	68.1 ± 4.9	0.9863
0.093	587.3 ± 64.0	192.3 ± 21.0	0.9820	0.064	126.7 ± 15.4	56.3 ± 6.8	0.9734
0.069	441.6 ± 89.4	144.6 ± 29.3	0.9696	0.031	95.4 ± 18.9	42.4 ± 8.4	0.9504
				-0.002	26.2 ± 11.5	11.6 ± 5.1	0.9272
2.7 GeV/c							
0.119	798.2 ± 41.9	273.0 ± 14.3	0.9974				
0.113	821.1 ± 33.1	280.8 ± 11.3	0.9943				
0.105	778.4 ± 33.5	266.2 ± 11.5	0.9899				
0.087	650.1 ± 64.7	222.3 ± 22.1	0.9804				
0.063	572.8 ± 106.9	195.9 ± 36.6	0.9671				

TABLE III. - continued

u (GeV/c) ²	$d\sigma/du$ $\mu\text{b}/(\text{GeV}/c)^2$	$d\sigma/d\Omega$ $\mu\text{b}/\text{sr}$	$-\cos\theta$ c.m.	u (GeV/c) ²	$d\sigma/du$ $\mu\text{b}/(\text{GeV}/c)^2$	$d\sigma/d\Omega$ $\mu\text{b}/\text{sr}$	$-\cos\theta$ c.m.
3.5 GeV/c				4.2 GeV/c			
0.093	167.5 ± 14.4	76.9 ± 6.6	0.9958	0.078	91.9 ± 13.6	51.7 ± 7.7	0.9945
0.088	157.1 ± 11.6	72.2 ± 5.3	0.9916	0.072	101.9 ± 7.4	57.3 ± 4.2	0.9891
0.079	132.6 ± 11.1	60.9 ± 5.1	0.9855	0.063	106.9 ± 8.0	60.1 ± 4.5	0.9812
0.061	112.9 ± 14.2	51.9 ± 6.5	0.9721	0.044	81.6 ± 10.6	45.9 ± 6.0	0.9641
0.027	81.9 ± 17.0	37.6 ± 7.8	0.9476	0.006	57.1 ± 11.9	32.1 ± 6.7	0.9311
-0.007	35.8 ± 12.1	16.4 ± 5.6	0.9233	-0.037	34.3 ± 8.2	19.3 ± 4.6	0.8931
3.6 GeV/c				4.3 GeV/c			
0.091	130.1 ± 16.8	61.7 ± 8.0	0.9958	0.076	100.7 ± 13.2	58.1 ± 7.6	0.9944
0.085	169.4 ± 13.0	80.3 ± 6.2	0.9914	0.070	103.3 ± 9.4	59.7 ± 5.4	0.9888
0.077	107.3 ± 11.6	50.9 ± 5.5	0.9850	0.061	75.2 ± 8.0	43.4 ± 4.6	0.9807
0.058	105.1 ± 14.9	49.8 ± 7.1	0.9711	0.042	64.2 ± 10.0	37.1 ± 5.8	0.9631
0.023	71.2 ± 15.7	33.8 ± 7.4	0.9454	0.004	49.0 ± 11.4	28.3 ± 6.6	0.9292
-0.011	41.6 ± 12.7	19.7 ± 6.0	0.9200	-0.039	26.5 ± 7.4	15.3 ± 4.3	0.8896
3.7 GeV/c				4.4 GeV/c			
0.089	160.3 ± 15.7	78.4 ± 7.7	0.9957	0.075	108.7 ± 9.2	64.4 ± 5.4	0.9942
0.083	129.6 ± 9.5	63.3 ± 4.6	0.9911	0.068	66.7 ± 5.9	39.5 ± 3.5	0.9884
0.074	122.3 ± 8.6	59.8 ± 4.2	0.9844	0.059	70.4 ± 5.3	41.7 ± 3.1	0.9800
0.055	115.2 ± 13.6	56.3 ± 6.6	0.9698	0.040	60.1 ± 7.7	35.6 ± 4.6	0.9619
0.020	82.4 ± 16.5	40.3 ± 8.1	0.9430	0.002	40.7 ± 8.6	24.1 ± 5.1	0.9270
-0.015	47.0 ± 13.5	23.0 ± 6.6	0.9162	-0.042	22.1 ± 5.5	13.1 ± 3.3	0.8853
3.8 GeV/c				4.5 GeV/c			
0.087	165.0 ± 9.7	83.1 ± 4.9	0.9956	0.073	62.4 ± 13.7	37.9 ± 8.3	0.9939
0.081	142.2 ± 6.6	71.6 ± 3.3	0.9908	0.067	72.5 ± 10.3	44.0 ± 6.3	0.9879
0.072	124.6 ± 6.0	62.7 ± 3.0	0.9839	0.058	62.4 ± 6.9	37.9 ± 4.2	0.9794
0.053	101.4 ± 11.2	51.1 ± 5.6	0.9689	0.038	51.4 ± 9.4	31.2 ± 5.7	0.9608
0.017	76.5 ± 14.5	38.5 ± 7.3	0.9408	0.000	39.0 ± 10.3	23.7 ± 6.3	0.9244
-0.019	47.2 ± 10.3	23.8 ± 5.2	0.9120	-0.047	19.5 ± 5.6	11.8 ± 3.4	0.8799
3.9 GeV/c				4.6 GeV/c			
0.084	168.5 ± 11.1	87.3 ± 5.8	0.9953	0.071	82.0 ± 13.0	51.0 ± 8.1	0.9936
0.078	132.5 ± 7.0	68.7 ± 3.6	0.9904	0.065	81.2 ± 6.7	50.5 ± 4.2	0.9875
0.070	112.3 ± 6.6	58.2 ± 3.4	0.9832	0.056	53.9 ± 5.3	33.5 ± 3.3	0.9787
0.050	107.2 ± 12.0	55.6 ± 6.2	0.9677	0.037	46.3 ± 7.0	28.8 ± 4.4	0.9598
0.015	56.8 ± 11.5	29.4 ± 6.0	0.9385	-0.001	30.0 ± 7.2	18.7 ± 4.5	0.9228
-0.024	46.9 ± 10.5	24.3 ± 5.4	0.9075	-0.049	14.8 ± 4.9	9.2 ± 3.0	0.8763
4.0 GeV/c				4.7 GeV/c			
0.082	115.0 ± 12.6	61.3 ± 6.7	0.9950	0.070	70.4 ± 9.6	44.8 ± 6.1	0.9943
0.076	134.9 ± 10.7	71.9 ± 5.7	0.9900	0.064	69.9 ± 5.7	44.5 ± 3.6	0.9878
0.067	94.6 ± 8.7	50.4 ± 4.6	0.9825	0.055	54.6 ± 4.0	34.8 ± 2.5	0.9786
0.048	75.6 ± 10.5	40.3 ± 5.6	0.9666	0.036	45.5 ± 6.3	29.0 ± 4.0	0.9600
0.012	52.3 ± 11.5	27.9 ± 6.1	0.9363	0.007	27.6 ± 7.5	17.6 ± 4.8	0.9309
-0.028	27.8 ± 8.6	14.8 ± 4.6	0.9028	4.8 GeV/c			
4.1 GeV/c				0.069	63.2 ± 7.9	41.2 ± 5.1	0.9940
0.080	135.0 ± 10.6	74.0 ± 5.8	0.9946	0.062	57.6 ± 5.5	37.5 ± 3.6	0.9874
0.074	124.8 ± 8.4	68.4 ± 4.6	0.9894	0.053	49.1 ± 4.5	32.0 ± 2.9	0.9780
0.065	98.2 ± 6.8	53.8 ± 3.7	0.9818	0.034	48.3 ± 6.5	31.5 ± 4.2	0.9585
0.046	85.3 ± 10.7	46.7 ± 5.9	0.9653	0.004	25.6 ± 7.3	16.7 ± 4.8	0.9278
0.009	63.0 ± 12.7	34.5 ± 7.0	0.9335				
-0.033	37.2 ± 8.3	20.4 ± 4.5	0.8973				

TABLE III - continued

u (GeV/c) ²	$d\sigma/du$ $\mu\text{b}/(\text{GeV}/c)^2$	$d\sigma/d\eta$ $\mu\text{b}/\text{sr}$	$-\cos \theta$ c.m.	u (GeV/c) ²	$d\sigma/du$ $\mu\text{b}/(\text{GeV}/c)^2$	$d\sigma/d\eta$ $\mu\text{b}/\text{sr}$	$-\cos \theta$ c.m.
4.9 GeV/c				5.4 GeV/c			
0.067	78.9 ± 11.1	52.6 ± 7.4	0.9938	0.061	61.4 ± 8.6	45.5 ± 6.4	0.9930
0.061	58.2 ± 5.9	38.8 ± 3.9	0.9870	0.055	46.1 ± 4.4	34.1 ± 3.3	0.9854
0.052	50.4 ± 4.8	33.6 ± 3.2	0.9775	0.045	46.3 ± 4.0	34.3 ± 3.0	0.9745
0.033	51.1 ± 6.7	34.0 ± 4.5	0.9575	0.026	31.2 ± 4.7	23.1 ± 3.5	0.9518
0.002	23.5 ± 6.1	15.7 ± 4.1	0.9251	-0.008	16.1 ± 4.7	11.9 ± 3.5	0.9124
5.0 GeV/c				5.6 GeV/c			
0.066	65.4 ± 8.8	44.5 ± 6.0	0.9936	0.059	49.0 ± 9.5	37.7 ± 7.3	0.9928
0.060	69.8 ± 6.0	47.5 ± 4.1	0.9868	0.052	40.4 ± 4.7	31.1 ± 3.6	0.9848
0.050	49.3 ± 4.8	33.6 ± 3.3	0.9768	0.043	34.9 ± 3.9	26.9 ± 3.0	0.9734
0.031	42.6 ± 6.4	29.0 ± 4.4	0.9565	0.023	24.3 ± 3.9	18.7 ± 3.0	0.9496
0.000	34.7 ± 9.2	23.6 ± 6.3	0.9227	-0.012	16.6 ± 5.0	12.8 ± 3.9	0.9074
5.1 GeV/c				5.8 GeV/c			
0.065	66.9 ± 6.9	46.6 ± 4.8	0.9935	0.057	48.5 ± 7.1	38.8 ± 5.7	0.9924
0.058	61.8 ± 5.5	43.0 ± 3.8	0.9865	0.050	29.9 ± 4.6	23.9 ± 3.7	0.9842
0.049	43.8 ± 4.3	30.5 ± 3.0	0.9763	0.041	32.5 ± 3.6	26.0 ± 2.9	0.9722
0.030	34.7 ± 5.0	24.1 ± 3.5	0.9554	0.021	23.2 ± 4.3	18.6 ± 3.4	0.9476
-0.002	34.5 ± 8.4	24.0 ± 5.8	0.9204	-0.015	12.5 ± 4.2	10.0 ± 3.4	0.9024
5.2 GeV/c				6.0 GeV/c			
0.064	57.9 ± 6.9	41.1 ± 4.9	0.9934	0.055	34.5 ± 7.1	28.6 ± 5.9	0.9919
0.057	50.7 ± 4.8	36.0 ± 3.4	0.9862	0.048	30.0 ± 4.1	24.9 ± 3.4	0.9834
0.048	37.6 ± 4.3	26.7 ± 3.1	0.9758	0.039	24.5 ± 3.6	20.3 ± 3.0	0.9709
0.029	29.8 ± 4.8	21.2 ± 3.4	0.9545	0.019	17.3 ± 3.4	14.4 ± 2.8	0.9454
-0.004	15.6 ± 4.3	11.1 ± 3.1	0.9183	-0.018	9.8 ± 3.0	8.1 ± 2.5	0.8969
5.3 GeV/c							
0.062	71.4 ± 7.9	51.8 ± 5.7	0.9932				
0.056	51.1 ± 5.6	37.1 ± 4.1	0.9858				
0.046	37.3 ± 5.4	27.1 ± 3.9	0.9751				
0.027	40.6 ± 6.3	29.5 ± 4.6	0.9531				
-0.006	16.5 ± 6.5	12.0 ± 4.7	0.9153				

TABLE IV. Angular distributions for the θ^F analysis.

u (GeV/c) ²	$d\sigma/du$ $\mu\text{b}/(\text{GeV}/c)^2$	$d\sigma/d\Omega$ $\mu\text{b}/\text{sr}$	$-\cos \theta$ c.m.	u (GeV/c) ²	$d\sigma/du$ $\mu\text{b}/(\text{GeV}/c)^2$	$d\sigma/d\Omega$ $\mu\text{b}/\text{sr}$	$-\cos \theta$ c.m.
2.0 GeV/c				2.8 GeV/c			
0.155	88.9 ± 58.5	21.4 ± 14.1	0.9984	0.114	657.8 ± 15.3	234.6 ± 5.5	0.9964
0.151	144.9 ± 25.8	34.8 ± 6.2	0.9970	0.107	638.0 ± 12.4	227.5 ± 4.4	0.9924
0.144	186.1 ± 29.2	44.7 ± 7.0	0.9945	0.094	579.2 ± 30.7	206.5 ± 10.9	0.9853
0.135	131.2 ± 28.2	31.5 ± 6.8	0.9909	0.077	494.5 ± 39.9	176.3 ± 14.2	0.9757
0.124	112.3 ± 26.8	27.0 ± 6.4	0.9867	0.057	419.1 ± 53.5	149.5 ± 19.1	0.9644
2.1 GeV/c				2.9 GeV/c			
0.149	16.6 ± 39.3	4.1 ± 9.7	0.9983	0.110	565.7 ± 23.7	210.0 ± 8.8	0.9960
0.144	73.5 ± 18.6	18.1 ± 4.6	0.9967	0.103	522.7 ± 19.8	194.0 ± 7.3	0.9918
0.137	93.1 ± 19.2	22.9 ± 4.7	0.9936	0.089	442.7 ± 31.7	164.3 ± 11.8	0.9841
0.126	89.8 ± 20.3	22.1 ± 5.0	0.9893	0.071	368.0 ± 36.4	136.6 ± 13.5	0.9736
0.114	94.5 ± 25.8	23.2 ± 6.3	0.9842	0.050	293.0 ± 45.9	108.8 ± 17.0	0.9611
2.2 GeV/c				3.0 GeV/c			
0.143	186.1 ± 71.0	50.1 ± 19.1	0.9981	0.106	422.5 ± 20.5	163.0 ± 7.9	0.9955
0.138	218.2 ± 36.5	58.8 ± 9.8	0.9962	0.098	394.8 ± 19.7	152.4 ± 7.6	0.9908
0.130	257.3 ± 41.6	69.3 ± 11.2	0.9927	0.084	289.0 ± 26.5	111.5 ± 10.2	0.9824
0.118	237.0 ± 38.1	63.8 ± 10.3	0.9879	0.065	269.9 ± 29.2	104.2 ± 11.3	0.9708
0.105	145.4 ± 38.1	39.2 ± 10.3	0.9821	0.042	222.7 ± 37.2	85.9 ± 14.4	0.9570
2.3 GeV/c				3.1 GeV/c			
0.137	491.6 ± 63.2	139.5 ± 17.9	0.9977	0.103	318.6 ± 20.0	127.6 ± 8.0	0.9952
0.132	565.2 ± 38.5	160.4 ± 10.9	0.9956	0.094	286.7 ± 17.0	114.9 ± 6.8	0.9898
0.123	459.0 ± 39.8	130.3 ± 11.3	0.9917	0.079	262.2 ± 23.5	105.0 ± 9.4	0.9804
0.111	421.1 ± 51.8	119.5 ± 14.7	0.9863	0.059	222.4 ± 28.8	89.1 ± 11.5	0.9675
0.097	277.9 ± 42.2	78.9 ± 12.0	0.9798	0.035	137.3 ± 27.5	55.0 ± 11.0	0.9524
2.4 GeV/c				3.2 GeV/c			
0.132	822.6 ± 54.9	245.4 ± 16.4	0.9976	0.099	268.8 ± 15.2	111.6 ± 6.3	0.9949
0.127	849.5 ± 40.2	253.4 ± 12.0	0.9951	0.090	220.8 ± 12.1	91.7 ± 5.0	0.9891
0.117	559.8 ± 45.8	167.0 ± 13.7	0.9907	0.075	164.6 ± 18.2	68.3 ± 7.6	0.9789
0.104	433.7 ± 58.1	129.4 ± 17.3	0.9847	0.053	138.3 ± 19.0	57.4 ± 7.9	0.9649
0.089	411.0 ± 59.3	122.6 ± 17.7	0.9776	0.028	116.2 ± 20.8	48.2 ± 8.6	0.9486
2.5 GeV/c				3.3 GeV/c			
0.127	871.3 ± 44.5	272.6 ± 13.9	0.9973	0.096	182.8 ± 15.0	78.6 ± 6.4	0.9946
0.121	807.1 ± 36.5	252.5 ± 11.4	0.9945	0.087	184.3 ± 10.4	79.2 ± 4.5	0.9882
0.111	730.3 ± 42.3	228.5 ± 13.2	0.9894	0.070	168.9 ± 16.5	72.6 ± 7.1	0.9770
0.097	582.6 ± 55.8	182.3 ± 17.5	0.9826	0.048	134.9 ± 18.7	58.0 ± 8.0	0.9616
0.081	483.0 ± 58.4	151.1 ± 18.3	0.9747	0.021	109.1 ± 18.4	46.9 ± 7.9	0.9438
2.6 GeV/c				3.4 GeV/c			
0.122	766.0 ± 54.9	250.8 ± 18.0	0.9968	0.093	173.0 ± 11.5	76.9 ± 5.1	0.9939
0.116	902.4 ± 43.0	295.4 ± 14.1	0.9937	0.083	144.9 ± 9.6	64.4 ± 4.3	0.9868
0.105	626.6 ± 49.5	205.1 ± 16.2	0.9880	0.065	152.2 ± 14.6	67.7 ± 6.5	0.9745
0.090	595.3 ± 64.7	194.9 ± 21.2	0.9804	0.041	82.9 ± 14.2	36.9 ± 6.3	0.9578
0.073	481.8 ± 70.5	157.7 ± 23.1	0.9716	0.014	66.8 ± 13.5	29.7 ± 6.0	0.9386
2.7 GeV/c				3.5 GeV/c			
0.118	812.3 ± 39.1	277.8 ± 13.4	0.9966	0.090	165.9 ± 10.0	76.2 ± 4.6	0.9932
0.111	767.5 ± 30.2	262.5 ± 10.3	0.9930	0.079	141.0 ± 10.3	64.8 ± 4.7	0.9855
0.099	688.6 ± 41.8	235.5 ± 14.3	0.9866	0.061	106.5 ± 13.1	48.9 ± 6.0	0.9723
0.083	669.6 ± 61.2	229.0 ± 20.9	0.9778	0.036	85.9 ± 14.3	39.5 ± 6.6	0.9543
0.064	581.7 ± 83.7	198.9 ± 28.6	0.9678	0.007	56.2 ± 11.9	25.8 ± 5.5	0.9335

TABLE IV. - continued

u (GeV/c) ²	$d\sigma/du$ $\mu\text{b}/(\text{GeV}/c)^2$	$d\sigma/d\Omega$ $\mu\text{b}/\text{sr}$	$-\cos\theta$ c.m.	u (GeV/c) ²	$d\sigma/du$ $\mu\text{b}/(\text{GeV}/c)^2$	$d\sigma/d\Omega$ $\mu\text{b}/\text{sr}$	$-\cos\theta$ c.m.
3.6 GeV/c				4.4 GeV/c			
0.087	147.3 ± 12.4	69.8 ± 5.9	0.9929	0.068	88.3 ± 5.2	52.3 ± 3.1	0.9882
0.076	144.3 ± 11.7	68.4 ± 5.5	0.9845	0.053	59.9 ± 5.3	35.5 ± 3.1	0.9737
0.057	83.1 ± 11.7	39.4 ± 5.5	0.9701	0.025	57.3 ± 7.2	33.9 ± 4.3	0.9482
0.031	69.0 ± 14.3	32.7 ± 6.8	0.9507	-0.010	28.4 ± 5.9	16.8 ± 3.5	0.9158
0.001	54.9 ± 12.4	26.0 ± 5.9	0.9288	-0.043	24.7 ± 5.7	14.6 ± 3.4	0.8848
3.7 GeV/c				4.5 GeV/c			
0.085	142.8 ± 11.7	69.8 ± 5.7	0.9926	0.065	69.5 ± 6.3	42.2 ± 3.8	0.9862
0.073	125.5 ± 7.9	61.3 ± 3.9	0.9837	0.047	55.6 ± 8.9	33.7 ± 5.4	0.9695
0.053	102.8 ± 11.4	50.2 ± 5.6	0.9682	0.018	43.6 ± 7.6	26.5 ± 4.6	0.9413
0.026	95.9 ± 15.2	46.9 ± 7.4	0.9472	-0.019	30.9 ± 8.8	18.8 ± 5.3	0.9064
-0.005	57.4 ± 11.0	28.0 ± 5.4	0.9240	-0.051	14.2 ± 5.1	8.6 ± 3.1	0.8753
3.8 GeV/c				4.6 GeV/c			
0.082	155.0 ± 6.7	78.1 ± 3.4	0.9919	0.063	72.7 ± 6.2	45.2 ± 3.9	0.9860
0.069	117.1 ± 6.1	59.0 ± 3.1	0.9820	0.046	54.1 ± 5.6	33.6 ± 3.5	0.9691
0.048	98.4 ± 9.6	49.6 ± 4.8	0.9650	0.016	36.9 ± 6.2	22.9 ± 3.9	0.9398
0.020	72.9 ± 11.0	36.7 ± 5.5	0.9425	-0.021	18.7 ± 4.5	11.6 ± 2.8	0.9036
-0.011	58.2 ± 9.0	29.3 ± 4.5	0.9182	-0.054	16.0 ± 5.4	9.9 ± 3.4	0.8715
3.9 GeV/c				4.7 GeV/c			
0.079	143.9 ± 7.0	74.6 ± 3.6	0.9913	0.067	73.2 ± 9.0	46.6 ± 5.7	0.9909
0.066	119.5 ± 7.0	61.9 ± 3.6	0.9806	0.061	60.9 ± 4.8	38.8 ± 3.1	0.9845
0.044	93.1 ± 9.5	48.2 ± 4.9	0.9623	0.049	55.3 ± 5.2	35.2 ± 3.3	0.9730
0.014	58.3 ± 9.5	30.2 ± 4.9	0.9383	0.033	37.5 ± 5.5	23.9 ± 3.5	0.9571
-0.017	47.9 ± 8.9	24.8 ± 4.6	0.9128	0.016	35.1 ± 7.3	22.3 ± 4.6	0.9394
4.0 GeV/c				4.8 GeV/c			
0.077	131.3 ± 9.0	70.0 ± 4.8	0.9906	0.065	62.0 ± 7.0	40.4 ± 4.6	0.9904
0.063	86.5 ± 8.0	46.1 ± 4.3	0.9791	0.059	55.2 ± 4.8	36.0 ± 3.1	0.9834
0.040	62.7 ± 8.8	33.4 ± 4.7	0.9595	0.046	50.4 ± 5.6	32.8 ± 3.6	0.9708
0.009	49.6 ± 10.6	26.4 ± 5.7	0.9340	0.029	35.9 ± 5.9	23.4 ± 3.8	0.9536
-0.023	37.0 ± 8.5	19.7 ± 4.5	0.9072	0.012	37.3 ± 7.4	24.3 ± 4.8	0.9354
4.1 GeV/c				4.9 GeV/c			
0.074	125.2 ± 6.9	68.6 ± 3.8	0.9897	0.064	75.0 ± 9.5	50.0 ± 6.3	0.9899
0.060	91.2 ± 7.0	50.0 ± 3.8	0.9773	0.057	59.4 ± 4.8	39.6 ± 3.2	0.9825
0.035	83.7 ± 9.8	45.9 ± 5.4	0.9560	0.044	47.3 ± 5.6	31.5 ± 3.7	0.9692
0.003	63.6 ± 10.5	34.8 ± 5.8	0.9286	0.027	41.6 ± 6.0	27.7 ± 4.0	0.9511
-0.029	32.3 ± 8.1	17.7 ± 4.4	0.9005	0.009	31.6 ± 6.1	21.1 ± 4.1	0.9327
4.2 GeV/c				5.0 GeV/c			
0.072	98.9 ± 7.0	55.6 ± 3.9	0.9890	0.062	78.4 ± 8.1	53.4 ± 5.5	0.9893
0.057	95.5 ± 7.9	53.7 ± 4.4	0.9757	0.055	55.8 ± 4.8	38.0 ± 3.3	0.9818
0.031	80.7 ± 10.4	45.4 ± 5.9	0.9528	0.042	48.3 ± 6.1	32.9 ± 4.2	0.9683
-0.002	43.6 ± 8.6	24.5 ± 4.8	0.9237	0.025	37.7 ± 6.5	25.7 ± 4.4	0.9496
-0.035	33.2 ± 7.7	18.7 ± 4.3	0.8947	0.006	34.8 ± 9.1	23.7 ± 6.2	0.9298
4.3 GeV/c				5.1 GeV/c			
0.070	104.1 ± 8.2	60.1 ± 4.7	0.9889	0.061	61.3 ± 6.4	42.7 ± 4.5	0.9890
0.055	62.8 ± 6.9	36.3 ± 4.0	0.9752	0.053	56.9 ± 4.1	39.6 ± 2.9	0.9807
0.029	60.6 ± 9.4	35.0 ± 5.4	0.9512	0.040	37.8 ± 4.5	26.3 ± 3.1	0.9661
-0.005	38.2 ± 8.3	22.1 ± 4.8	0.9205	0.021	39.0 ± 6.1	27.1 ± 4.2	0.9459
-0.038	39.3 ± 10.2	22.7 ± 5.9	0.8904	0.003	30.6 ± 7.2	21.3 ± 5.0	0.9254

TABLE IV. - continued

u (GeV/c) ²	$d\sigma/du$ $\mu\text{b}/(\text{GeV}/c)^2$	$d\sigma/d\Omega$ $\mu\text{b}/\text{sr}$	$-\cos \theta$ c.m.	u (GeV/c) ²	$d\sigma/du$ $\mu\text{b}/(\text{GeV}/c)^2$	$d\sigma/d\Omega$ $\mu\text{b}/\text{sr}$	$-\cos \theta$ c.m.
5.2 GeV/c				5.6 GeV/c			
0.059	57.8 ± 5.9	41.1 ± 4.2	0.9888	0.054	45.4 ± 6.4	35.0 ± 4.9	0.9871
0.052	38.8 ± 4.0	27.6 ± 2.8	0.9800	0.045	34.9 ± 3.5	26.9 ± 2.7	0.9757
0.038	34.0 ± 4.5	24.2 ± 3.2	0.9647	0.028	27.8 ± 3.7	21.4 ± 2.8	0.9557
0.019	27.7 ± 5.0	19.7 ± 3.6	0.9435	0.006	17.9 ± 4.2	13.8 ± 3.2	0.9290
0.000	15.0 ± 4.5	10.7 ± 3.2	0.9222	-0.012	17.4 ± 6.7	13.4 ± 5.2	0.9066
5.3 GeV/c				5.8 GeV/c			
0.058	60.5 ± 6.0	43.9 ± 4.4	0.9883	0.052	35.0 ± 5.1	28.0 ± 4.1	0.9861
0.050	50.2 ± 4.8	36.4 ± 3.5	0.9789	0.042	36.3 ± 3.4	29.0 ± 2.7	0.9734
0.035	36.7 ± 6.3	26.6 ± 4.6	0.9623	0.024	28.6 ± 4.0	22.9 ± 3.2	0.9512
0.015	31.0 ± 6.6	22.5 ± 4.8	0.9396	0.001	12.1 ± 5.1	9.7 ± 4.1	0.9219
-0.004	19.0 ± 7.4	13.8 ± 5.4	0.9175	-0.017	7.1 ± 4.2	5.7 ± 3.4	0.9002
5.4 GeV/c				6.0 GeV/c			
0.057	46.3 ± 6.1	34.3 ± 4.5	0.9879	0.049	34.6 ± 4.5	28.7 ± 3.7	0.9850
0.048	51.0 ± 3.9	37.8 ± 2.9	0.9778	0.039	21.5 ± 3.3	17.8 ± 2.7	0.9710
0.033	33.7 ± 4.3	25.0 ± 3.2	0.9600	0.020	16.3 ± 3.3	13.5 ± 2.7	0.9465
0.012	22.8 ± 4.3	16.9 ± 3.2	0.9358	-0.005	13.6 ± 3.1	11.3 ± 2.6	0.9145
-0.008	19.9 ± 5.5	14.7 ± 4.1	0.9128	-0.020	10.3 ± 3.9	8.5 ± 3.2	0.8941

the angular distributions obtained in the θ^F analysis. Slopes and intercepts for each of the analyses are given in Table V.

For incident pion momenta of 4.4 and 4.6 GeV/c data were obtained at each of the two spectrometer geometries so that consistency checks could be made. The good agreement between the two settings is shown in Table VI where the slopes and intercepts obtained at the low momentum geometry (2.0 - 4.6 GeV/c) are compared with those from the high momentum geometry (4.4 - 6.0 GeV/c). The values reported in Table V for 4.4 GeV/c and 4.6 GeV/c for each analysis are averages of the values from the two geometries. However, the angular distributions for these two points in Table III and IV correspond to the low momentum geometry. The low momentum data are presented rather than the high momentum data because they cover a wider u range and have better statistical accuracy.

Finally, the averages of the θ^F and θ^B slopes and intercepts from Table V are listed in Table VII and plotted in Figures 17 and 18. These are the values that have already appeared as published results of this experiment^{24,25}. Several interpretations of the structure observed in the energy dependence of the backward cross section (Figure 18) will be discussed in Chapter IV. The deep dip seen at ~2.1 GeV/c is emphasized even more in Figure 19, which contains data from two other experiments in the region near 2.1 GeV/c.

TABLE V. Slopes and intercepts obtained in the θ^F and θ^B analyses.

θ^B Analysis					θ^F Analysis				
P_π (GeV/c)	$\frac{d\sigma}{d\Omega}(180^\circ)$ ($\mu\text{b/sr}$)	Slope (GeV/c) $^{-2}$	$\frac{d\sigma}{d\Omega}(180^\circ)$ ($\mu\text{b/sr}$)	Slope (GeV/c) $^{-2}$	P_π (GeV/c)	$\frac{d\sigma}{d\Omega}(180^\circ)$ ($\mu\text{b/sr}$)	Slope (GeV/c) $^{-2}$	$\frac{d\sigma}{d\Omega}(180^\circ)$ ($\mu\text{b/sr}$)	Slope (GeV/c) $^{-2}$
2.0	$44.4^{+10.1}_{-8.2}$	12.9 ± 10.9	$43.5^{+9.8}_{-8.0}$	11.2 ± 10.2	3.9	$82.2^{+3.7}_{-3.7}$	12.3 ± 1.7	$84.3^{+4.4}_{-4.2}$	12.3 ± 1.6
2.1	$17.9^{+6.0}_{-4.5}$	-5.8 ± 13.7	$18.7^{+5.8}_{-4.4}$	-6.6 ± 11.5	4.0	$74.4^{+5.3}_{-4.8}$	14.0 ± 2.2	$75.3^{+5.7}_{-5.3}$	14.1 ± 2.0
2.2	$74.4^{+14.5}_{-12.1}$	9.8 ± 8.2	$68.4^{+13.9}_{-11.6}$	6.5 ± 8.0	4.1	$75.4^{+4.1}_{-3.9}$	11.4 ± 1.7	$75.4^{+4.7}_{-4.5}$	11.1 ± 1.7
2.3	$183.4^{+15.6}_{-14.6}$	16.6 ± 4.5	$179.0^{+15.0}_{-13.8}$	16.1 ± 3.9	4.2	$66.6^{+4.4}_{-4.2}$	9.4 ± 1.9	$66.5^{+5.0}_{-4.7}$	9.9 ± 1.8
2.4	$291.3^{+16.5}_{-15.5}$	22.9 ± 3.4	$292.6^{+16.4}_{-15.6}$	21.4 ± 3.2	4.3	$62.9^{+5.0}_{-4.7}$	11.7 ± 2.2	$61.5^{+5.3}_{-4.9}$	10.6 ± 2.0
2.5	$320.7^{+14.7}_{-14.3}$	16.7 ± 2.8	$293.5^{+13.7}_{-13.1}$	12.8 ± 2.3	4.4	$57.4^{+5.4}_{-4.7}$	14.0 ± 4.1	$58.4^{+6.0}_{-4.4}$	13.8 ± 2.9
2.6	$313.9^{+18.5}_{-17.4}$	13.3 ± 3.0	$311.5^{+18.2}_{-17.2}$	12.6 ± 2.7	4.5	$47.4^{+5.0}_{-4.6}$	10.3 ± 2.4	$50.1^{+5.5}_{-5.0}$	11.5 ± 2.3
2.7	$294.1^{+13.1}_{-12.6}$	6.2 ± 2.5	$285.2^{+12.7}_{-12.1}$	6.2 ± 2.1	4.6	$51.8^{+4.4}_{-4.1}$	14.8 ± 3.5	$51.7^{+4.7}_{-4.3}$	14.2 ± 2.9
2.8	$261.5^{+6.6}_{-6.5}$	9.4 ± 1.7	$249.4^{+6.2}_{-6.1}$	7.6 ± 1.5	4.7	$50.7^{+4.6}_{-4.3}$	15.3 ± 3.7	$50.7^{+5.3}_{-4.8}$	15.1 ± 3.7
2.9	$230.0^{+10.1}_{-9.2}$	11.4 ± 2.4	$226.7^{+9.4}_{-9.0}$	11.3 ± 2.0	4.8	$42.7^{+4.1}_{-3.9}$	10.8 ± 3.7	$43.6^{+4.6}_{-4.1}$	10.9 ± 3.5
3.0	$178.4^{+9.0}_{-8.4}$	11.7 ± 2.4	$176.9^{+8.7}_{-8.3}$	11.4 ± 2.0	4.9	$48.8^{+5.0}_{-4.6}$	13.4 ± 3.7	$51.9^{+5.5}_{-5.0}$	14.8 ± 3.4
3.1	$132.7^{+8.6}_{-8.1}$	7.4 ± 2.9	$137.8^{+8.5}_{-8.0}$	10.0 ± 2.3	5.0	$50.1^{+4.7}_{-4.3}$	12.8 ± 3.7	$54.6^{+5.8}_{-5.3}$	15.7 ± 3.8
3.2	$114.3^{+6.3}_{-6.1}$	13.0 ± 2.3	$118.0^{+6.6}_{-6.2}$	13.3 ± 2.1	5.1	$47.6^{+4.1}_{-3.7}$	13.9 ± 3.3	$48.2^{+4.7}_{-4.3}$	13.4 ± 3.4
3.3	$90.8^{+5.6}_{-5.3}$	8.9 ± 2.2	$87.7^{+5.8}_{-5.4}$	6.9 ± 2.1	5.2	$44.9^{+4.3}_{-3.9}$	19.6 ± 3.8	$44.5^{+5.0}_{-4.5}$	19.1 ± 3.8
3.4	$85.6^{+5.3}_{-5.0}$	12.0 ± 2.5	$84.4^{+5.6}_{-5.3}$	11.1 ± 2.2	5.3	$50.3^{+5.1}_{-4.9}$	17.6 ± 4.3	$51.1^{+5.9}_{-5.3}$	17.5 ± 4.3
3.5	$82.5^{+5.3}_{-4.9}$	12.9 ± 2.3	$85.2^{+5.5}_{-5.2}$	13.1 ± 2.1	5.4	$46.9^{+4.6}_{-4.3}$	17.2 ± 3.8	$48.2^{+5.4}_{-4.8}$	17.4 ± 3.6
3.6	$79.9^{+6.0}_{-5.5}$	12.8 ± 2.4	$82.5^{+6.8}_{-6.3}$	13.4 ± 2.4	5.6	$38.4^{+4.7}_{-4.1}$	16.0 ± 4.2	$38.9^{+5.4}_{-4.8}$	16.6 ± 4.2
3.7	$74.7^{+4.7}_{-4.4}$	9.4 ± 2.1	$75.1^{+5.4}_{-5.0}$	9.0 ± 1.9	5.8	$37.3^{+4.6}_{-4.1}$	17.3 ± 4.4	$39.0^{+6.3}_{-5.4}$	16.4 ± 5.5
3.8	$83.0^{+3.4}_{-3.3}$	11.8 ± 1.6	$83.0^{+3.8}_{-3.7}$	11.2 ± 1.4	6.0	$30.9^{+4.3}_{-3.7}$	17.6 ± 4.4	$31.0^{+4.6}_{-4.0}$	17.3 ± 3.9

TABLE VII. Slope parameters and differential cross sections at 180° for π^+p backward elastic scattering.

P_π (GeV/c)	\sqrt{s} (MeV)	$\frac{d\sigma}{d\Omega}(180^\circ)$ ($\mu\text{b/sr}$)	$\frac{d\sigma}{d\Omega}(180^\circ)$ ($\mu\text{b/GeV}^2$)	Slope (GeV/c) $^{-2}$	P_π (GeV/c)	\sqrt{s} (MeV)	$\frac{d\sigma}{d\Omega}(180^\circ)$ ($\mu\text{b/sr}$)	$\frac{d\sigma}{d\Omega}(180^\circ)$ ($\mu\text{b/GeV}^2$)	Slope (GeV/c) $^{-2}$
2.0	2159	$44.0^{+10.1}_{-8.2}$	183^{+42}_{-34}	12.1 ± 10.2	3.9	2867	$83.3^{+3.7}_{-3.7}$	161^{+7}_{-7}	12.3 ± 1.6
2.1	2202	$18.3^{+6.0}_{-4.5}$	74^{+24}_{-18}	-6.2 ± 11.5	4.0	2900	$74.8^{+5.3}_{-4.8}$	140^{+10}_{-9}	14.0 ± 2.0
2.2	2244	$71.5^{+14.5}_{-12.1}$	266^{+54}_{-45}	8.1 ± 8.0	4.1	2932	$75.4^{+4.1}_{-3.9}$	138^{+7}_{-7}	11.2 ± 1.7
2.3	2286	$181.2^{+15.6}_{-14.6}$	638^{+55}_{-51}	16.3 ± 3.9	4.2	2964	$66.6^{+4.4}_{-4.2}$	118^{+8}_{-7}	9.6 ± 1.8
2.4	2326	$291.9^{+16.5}_{-15.5}$	979^{+55}_{-52}	22.2 ± 3.2	4.3	2995	$62.3^{+5.0}_{-4.7}$	108^{+9}_{-8}	11.2 ± 2.0
2.5	2366	$307.2^{+14.7}_{-14.3}$	982^{+47}_{-46}	14.8 ± 2.3	4.4	3026	$57.8^{+5.4}_{-4.7}$	$97.6^{+9.1}_{-7.9}$	13.9 ± 2.9
2.6	2405	$312.6^{+18.5}_{-17.4}$	955^{+57}_{-53}	13.0 ± 2.7	4.5	3057	$48.8^{+5.0}_{-4.6}$	$80.4^{+8.2}_{-7.6}$	10.9 ± 2.3
2.7	2444	$289.6^{+13.1}_{-12.6}$	847^{+38}_{-37}	6.2 ± 2.1	4.6	3088	$51.8^{+4.4}_{-4.1}$	$83.3^{+7.1}_{-6.6}$	14.5 ± 2.9
2.8	2482	$255.5^{+6.6}_{-6.5}$	716^{+19}_{-18}	8.5 ± 1.5	4.7	3118	$50.7^{+4.6}_{-4.3}$	$79.6^{+7.2}_{-6.8}$	15.2 ± 3.7
2.9	2520	$228.2^{+10.1}_{-9.2}$	615^{+27}_{-25}	11.3 ± 2.0	4.8	3148	$43.2^{+4.1}_{-3.9}$	$66.3^{+6.3}_{-6.0}$	10.8 ± 3.5
3.0	2556	$177.7^{+9.0}_{-8.4}$	460^{+23}_{-22}	11.6 ± 2.0	4.9	3177	$50.4^{+5.0}_{-4.6}$	$75.7^{+7.5}_{-6.9}$	14.1 ± 3.4
3.1	2592	$135.2^{+8.6}_{-8.1}$	337^{+21}_{-20}	8.7 ± 2.3	5.0	3207	$52.3^{+4.7}_{-4.3}$	$76.8^{+6.9}_{-6.3}$	14.2 ± 3.8
3.2	2628	$116.2^{+6.3}_{-6.1}$	280^{+15}_{-15}	13.2 ± 2.1	5.1	3236	$47.9^{+4.1}_{-3.7}$	$68.8^{+5.9}_{-5.3}$	13.7 ± 3.4
3.3	2664	$89.3^{+5.6}_{-5.3}$	208^{+13}_{-12}	7.9 ± 2.1	5.2	3265	$44.7^{+4.3}_{-3.9}$	$62.9^{+6.0}_{-5.4}$	19.3 ± 3.8
3.4	2699	$85.0^{+5.3}_{-5.0}$	191^{+12}_{-11}	11.5 ± 2.2	5.3	3293	$50.7^{+5.1}_{-4.9}$	$69.9^{+7.0}_{-6.8}$	17.5 ± 4.3
3.5	2733	$83.8^{+5.3}_{-4.9}$	182^{+12}_{-11}	13.0 ± 2.1	5.4	3322	$47.6^{+4.6}_{-4.3}$	$64.3^{+6.2}_{-5.8}$	17.3 ± 3.6
3.6	2767	$81.2^{+6.0}_{-5.5}$	171^{+13}_{-12}	13.1 ± 2.4	5.6	3378	$38.7^{+4.7}_{-4.1}$	$50.3^{+6.1}_{-5.3}$	16.3 ± 4.2
3.7	2801	$74.9^{+4.7}_{-4.4}$	153^{+10}_{-9}	9.2 ± 1.9	5.8	3433	$38.2^{+4.6}_{-4.1}$	$47.8^{+5.8}_{-5.1}$	16.8 ± 5.5
3.8	2834	$83.0^{+3.4}_{-3.3}$	165^{+7}_{-7}	11.5 ± 1.4	6.0	3487	$30.9^{+4.3}_{-3.7}$	$37.3^{+5.2}_{-4.5}$	17.5 ± 3.9

Figure 17. Energy dependence of the slope of the backward peak in π^+p elastic scattering. These are the averages of the slopes obtained in the θ^B and θ^F analyses.

Figure 18. Energy dependence of the 180° differential cross section in π^+p elastic scattering. These are the averages of the intercepts obtained in the θ^F and θ^B analyses.

Figure 19. Energy dependence of the 180° differential cross section in π^+p elastic scattering. The data from Figure 18 are shown with data from ARIZONA [26] and BNL-ROCHESTER [6].

CHAPTER IV

INTERPRETATION OF EXPERIMENTAL RESULTS

4.1 INTRODUCTION

The clear correlation between the peaks observed in the energy dependence of the backward cross section and the position of known resonances has influenced the formulation of several models for backward scattering, including the resonance model and the interference model. In the former model the scattering amplitude for $\pi^+ p$ scattering is written as a sum of Breit-Wigner amplitudes corresponding to resonances having isospin $I = 3/2$. The latter model also includes Breit-Wigner amplitudes but superposes these resonant amplitudes on a nonresonant background, which is usually written in terms of a Regge amplitude. That is, in the resonance model it is assumed that the scattering mechanism involves resonance formation in the direct channel and the energy dependence of the backward cross section is expected to exhibit structure because the probability of resonance formation is intimately related to the total amount of available center-of-mass energy. On the other hand, the Regge model has had some success in explaining the dip in the $\pi^+ p$ elastic differential cross section at $u \sim -0.15 (\text{GeV}/c)^2$ by assuming that the scattering mechanism involves the crossed-channel exchange of the N and Δ Regge trajectories. For this reason, in the interference model it is assumed that the backward scattering amplitude includes both the direct and crossed-channel

mechanisms, as is illustrated in Figure 20. However, there is still some question as to how to take into account the contributions from both mechanisms. It has been pointed out^{27,28} that an amplitude written as a simple sum of Breit-Wigner amplitudes and a full Regge amplitude can involve double counting. For the case of π^+p backward elastic scattering a solution to this problem was proposed by Ma and Shaw²⁹. They identify the sum of the direct channel resonances with the signed part of the Regge amplitude and associate the purely real, nonsigned part with an interfering background. Thus, they write the scattering amplitude as a sum of Breit-Wigner amplitudes and only the non-signed part of the Regge amplitude. The data shown in Figure 18 were interpreted using both a pure resonance model and an interference model similar to that of Ma and Shaw.

4.2 THE RESONANCE MODEL

The spin-flip and non-flip parts of the resonance amplitude were parameterized as follows:

$$(\text{non-flip}) F_{\text{res}} = \frac{1}{k} \sum_n \frac{C_n X_n (J_n + 1/2)}{\epsilon_n - i} P_\ell(\cos \theta) \quad (1)$$

$$(\text{spin-flip}) G_{\text{res}} = \frac{1}{k} \sum_n \frac{C_n X_n (-1)^{J_n - \ell + 1/2}}{\epsilon_n - i} \frac{dP_\ell(\cos \theta)}{d(\cos \theta)} \quad (2)$$

where k is the center-of-mass momentum, C_n is a Clebsch-Gordan coefficient which equals one for π^+p resonances, θ is the center-of-mass

Figure 20. Schematic representation of the direct-channel and crossed-channel amplitudes. The resonance model includes only the direct channel but the interference model includes both amplitudes.

scattering angle, J_n is the spin of the resonance, X_n is its elasticity, $\epsilon_n = (M_n^2 - s)/M_n \Gamma_n$, s is the square of the energy in the center-of-mass, M_n is the mass of the resonance, and Γ_n is its full width. The effects of the Breit-Wigner tails for each resonance at mass values far away from M_n were decreased by multiplying each resonance amplitude by the factor $\exp(-d\epsilon_n^2)$, where d is a dimensionless cutoff parameter. Figure 21 illustrates the effect of this factor on a Breit-Wigner curve for the $\Delta(2850)$ resonance.

4.3 THE INTERFERENCE MODEL

Following a procedure used by other authors^{30, 31} Ma and Shaw³² write the spin-flip and non-flip parts of the Regge amplitude for pion-nucleon scattering as:

$$\text{(non-flip)} \quad F_{\text{Reg}}(\sqrt{s}, u) = f_1(\sqrt{s}, u) - (\cos \theta) f_1(-\sqrt{s}, u) \quad (3)$$

$$\text{(spin-flip)} \quad G_{\text{Reg}}(\sqrt{s}, u) = f_1(-\sqrt{s}, u) \quad (4)$$

where the f_1 amplitude for the j -th Regge trajectory is

$$f_1(\pm\sqrt{u}, s) = \frac{\gamma_j^\pm}{\pm\sqrt{u}} \frac{(E_u \pm M)(1 + \tau_j e^{-i\pi(\alpha_j - 1/2)})}{\Gamma(\alpha_j + 1/2) \cos \pi\alpha_j} \left(\frac{s}{s_j} \right)^{\alpha_j - 1/2} \quad (5)$$

The α_j , γ_j and s_j are parameterized as²⁹:

$$\gamma_N^+ = -11.7(1 - 1.25\sqrt{u}) \text{ GeV}^{-1}$$

$$\gamma_N^- = +11.7(1 + 1.25\sqrt{u}) \text{ GeV}^{-1}$$

$$\alpha_N = -0.35 - 0.09\sqrt{u} + 1.07u$$

$$s_N = 1.0 \text{ GeV}^2$$

Figure 21. Breit-Wigner curve for the Δ (2850) using three different values for the exponential damping factor, d . For this calculation the Δ (2850) was assigned a mass of 2889 MeV/c² and a full width of 406 MeV/c². The product $X(J + 1/2)$ was taken to be 0.29.

$$\begin{aligned}
\gamma_{\Delta}^{+} &= +0.186 (1 + 1.6\sqrt{u}) \text{ GeV}^{-1} \\
\gamma_{\Delta}^{-} &= -0.186 (1 - 1.6\sqrt{u}) \text{ GeV}^{-1} \\
\alpha_{\Delta} &= +0.14 + 0.89u \\
s_{\Delta} &= +1.7 \text{ GeV}^2.
\end{aligned}$$

The signature factor τ_j is -1 for the Δ trajectory and +1 for the N trajectory. The term containing this factor is called the signed part of the amplitude. It is not used in the interference model but is included here so that a comparison may be made between a fit obtained using only the total Regge amplitude and those obtained using the interference model amplitudes.

The amplitudes $f_1(\pm\sqrt{u}, s)$ given in (5) are related to those in (3) and (4) by the crossing symmetry relation:

$$f_1(\sqrt{s}, u) = \frac{E_s + M}{2\sqrt{s}} \left[\frac{(\sqrt{u} - \sqrt{s} + 2M)}{E_u + M} f_1(\sqrt{u}, s) + \frac{(\sqrt{u} + \sqrt{s} - 2M)}{E_u - M} f_1(-\sqrt{u}, s) \right] \quad (6)$$

where the center-of-mass energy of the nucleon is given by

$E_s = (s + M^2 - \mu^2) / 2\sqrt{s}$ and a corresponding definition holds for E_u . The

masses of the proton and pion are represented by M and μ , respec-

tively. Thus equation (6) may be used to transform (5) into forms

which can be directly substituted into (3) and (4). The cross section

obtained using equations (3) through (6) has a smooth energy dependence

and fits the data only in an average sense, as is shown in Figure 22. It

is clear that the Regge amplitude alone cannot account for the structure

Figure 22. Regge model fit to the data, including both the
signed and non-signed parts of the Regge amplitude.

observed in this energy region. Much better fits to the data were obtained by eliminating the signatured part of the Regge amplitude and writing the total amplitude as a sum of the non-signatured part of the Regge amplitude and the resonance amplitudes described in Section 4.2. This elimination of the signatured term is the defining characteristic of Ma and Shaw's interference model, which is based on the assumption that the signatured part can be identified with the sum of the direct-channel resonances. One may include the contribution of these resonances either by parameterizing them in terms of their Breit-Wigner amplitudes or by including the signatured term in the Regge amplitude. Inclusion of both the signatured term and the Breit-Wigner amplitudes would involve double counting. Thus, the total interference model amplitude used in making the fits described below included contributions from (1) and (2) as well as (3) and (4):

$$\frac{1}{(\hbar c)^2} \frac{d\sigma}{d\Omega} = (F_{\text{res}} + F'_{\text{Reg}})^2 + \sin^2\theta (G_{\text{res}} + G'_{\text{Reg}})^2 \quad (7)$$

where the prime on the amplitudes indicates that they were calculated without the contribution from the signatured term.

4.4 METHOD OF FITTING

A multiparameter maximum likelihood fitting program was used to fit the data shown in Figure 18. The fit parameters were the parameters of the Δ^{++} resonances having masses between 2170 and 3490

$\chi^2 \sim 15$ for 26 degrees of freedom³³.

Special attention was also given to fitting in the region near the $\Delta(3230)$ because of the uncertainty introduced by the lack of experimental data above 6.0 GeV/c. The $\Delta(3230)$ is the fifth recurrence on a Regge trajectory which also includes the $\Delta(1236)$, $\Delta(1950)$, $\Delta(2420)$, and $\Delta(2850)$. The sixth recurrence has not been observed, but its parameters can be inferred by extrapolation using expressions which relate the parameters of the observed recurrences on this trajectory³⁴. Hence, the existence of a $\Delta(3540)$ was hypothesized and its parameters were included in the fixed input to the fitting program. The difference between the best fit parameters for fits including and excluding this resonance was not significant.

4.5 DISCUSSION OF RESULTS OF FITTING

Figure 23 shows two curves describing the imaginary part of the resonance amplitude for fits including the one-star resonances and having a cutoff of 0.01. The upper curve gave a good fit for the interference model and the lower corresponds to a good fit using the resonance model. Similar curves for the real part of the resonance amplitude are shown in Figure 24. The dashed line in each figure corresponds to the real or imaginary part of the total (signed plus non-signed) Regge amplitude. The situation for the other fits using a different cutoff value or excluding the one-star resonances is similar, and this case was chosen simply to illustrate the different amplitudes

Figure 23. Imaginary part of the π^+p scattering amplitude for the resonance, Regge, and interference models. The curves for the resonance and interference models were obtained from fits which included the one-star resonances and had a cutoff, $d=0.01$. The dashed curve was obtained from equations (3), (5), and (6) without varying any parameters.

Figure 24. Real part of the π^+p scattering amplitude for the resonance Regge, and interference models. The curves for the resonance and interference models were obtained from fits which included the one-star resonances and had a cutoff, $d=0.01$. The dashed curve was obtained from equations (3), (5), and (6) without varying any parameters, and includes contributions from both the signed and non-signed parts of the Regge amplitude.

resulting from the two different models. Table IX lists the best fit parameters for each of eight fits. The parameters obtained for the pure resonance model differ from those of the interference model, particularly for the product $X(J + 1/2)$. Hence, two separate averages were taken, one for the four resonance model fits and one for the interference model fits. These averages, together with their systematic and statistical errors are presented in Table X. The systematic error associated with each parameter is the rms deviation of the central values of the four fits for that model. The statistical error on a given parameter was obtained by perturbing that parameter about its optimal value and refitting the remaining parameters. This process was continued until the χ^2 of the new fit differed from that of the best fit by an amount corresponding to one standard deviation³⁵. For the interference model fit using a cutoff of 0.10 it was found that fits in which the elasticity of the $\Delta(3230)$ was negative or zero could have χ^2 values within one standard deviation of the best fit value. Though the "best fit" values for these parameters are listed in Table IX they were not included in the calculation of the average values or in the determination of the quoted errors. Figure 25 shows a resonance model fit to the data for the case having $d = 0.10$ and excluding the one-star resonances. This curve is not significantly different from those obtained for each of the other seven fits. The dashed line shows the best fit possible if the $\Delta(2200)$ is excluded.

TABLE IX. Best fit values for parameters describing the Δ (2200), Δ (2420), Δ (2850) and Δ (3230). Eight different fits were obtained, corresponding to whether or not the 1^* resonances were included, whether or not the non-signatured part of the Regge amplitude was included, and two choices of an exponential resonance damping factor, d . The χ^2 for each fit was ≤ 16 for 26 degrees of freedom.

	<u>1*Resonance</u>	<u>Regge</u>	<u>d</u>	<u>Δ(2200)</u>	<u>Δ(2420)</u>	<u>Δ(2850)</u>	<u>Δ(3230)</u>
Mass (MeV/c ²)	No	Yes	.01	2243	2473	2949	3444
	No	No	.01	2179	2385	2876	3269
	Yes	Yes	.01	2220	2475	2951	3457
	Yes	No	.01	2182	2390	2877	3269
	No	Yes	.10	2282	2543	2959	3392 ^a
	No	No	.10	2215	2405	2884	3312
	Yes	Yes	.10	2246	2535	2974	3366 ^a
	Yes	No	.10	2202	2421	2885	3313
Width (MeV/c ²)	No	Yes	.01	234	461	288	637
	No	No	.01	337	479	369	614
	Yes	Yes	.01	273	459	266	683
	Yes	No	.01	279	483	358	644
	No	Yes	.10	144	348	367	347 ^a
	No	No	.10	324	490	398	725
	Yes	Yes	.10	240	354	287	272 ^a
	Yes	No	.10	281	480	404	712
$X(J + 1/2)$	No	Yes	.01	.51	.59	.15	.25
	No	No	.01	.84	1.02	.28	.39
	Yes	Yes	.01	.75	.61	.14	.19
	Yes	No	.01	1.08	1.00	.27	.40
	No	Yes	.10	.34	.38	.16	.10 ^a
	No	No	.10	.60	.94	.29	.49
	Yes	Yes	.10	.46	.32	.13	.06 ^a
	Yes	No	.10	.78	.90	.30	.48

^a This entry is not statistically significant and was not included in the calculation of the average and the mean statistical error.

TABLE X. Comparison of the results of fitting using the resonance (R) and interference (I) models. For each parameter two averages are presented, one for the four resonance model fits and one for the interference model fits.

	<u>Model</u>	<u>Mass (MeV/c²)</u>	<u>Width (MeV/c²)</u>	<u>X (J + 1/2)</u>
Δ (2200)	R	2194 $\begin{smallmatrix} + 31 \\ - 26 \end{smallmatrix} \pm 15^a$	305 $\pm 120 \pm 26$.82 $\begin{smallmatrix} +.36 \\ -.21 \end{smallmatrix} \pm .17$
	I	2248 $\begin{smallmatrix} + 19 \\ - 17 \end{smallmatrix} \pm 22$	223 $\begin{smallmatrix} +126 \\ - 58 \end{smallmatrix} \pm 48$.52 $\begin{smallmatrix} +.23 \\ -.10 \end{smallmatrix} \pm .15$
Δ (2420)	R	2400 $\pm 48 \pm 14$	483 $\pm 75 \pm 4$.96 $\begin{smallmatrix} +.37 \\ -.16 \end{smallmatrix} \pm .05$
	I	2506 $\begin{smallmatrix} + 17 \\ - 87 \end{smallmatrix} \pm 33$	406 $\begin{smallmatrix} + 150 \\ - 77 \end{smallmatrix} \pm 55$.47 $\begin{smallmatrix} +.25 \\ -.11 \end{smallmatrix} \pm .13$
Δ (2850)	R	2880 $\begin{smallmatrix} + 21 \\ - 23 \end{smallmatrix} \pm 4$	382 $\begin{smallmatrix} + 120 \\ - 180 \end{smallmatrix} \pm 19$.28 $\begin{smallmatrix} +.12 \\ -.18 \end{smallmatrix} \pm .01$
	I	2958 $\begin{smallmatrix} + 45 \\ - 42 \end{smallmatrix} \pm 10$	302 $\begin{smallmatrix} + 233 \\ - 174 \end{smallmatrix} \pm 39$.14 $\begin{smallmatrix} +.04 \\ -.08 \end{smallmatrix} \pm .02$
Δ (3230)	R	3291 $\begin{smallmatrix} + 56 \\ - 55 \end{smallmatrix} \pm 22$	674 $\begin{smallmatrix} + 1000 \\ - 280 \end{smallmatrix} \pm 46$.44 $\begin{smallmatrix} +.04 \\ -.08 \end{smallmatrix} \pm .05$
	I	3450 $\begin{smallmatrix} + 140 \\ - 68 \end{smallmatrix} \pm 6$	660 $\begin{smallmatrix} + 2730 \\ - 220 \end{smallmatrix} \pm 23$.22 $\begin{smallmatrix} +.05 \\ -.06 \end{smallmatrix} \pm .03$

^a The errors on the parameters are given in two parts. The first is the statistical error which was obtained as described in the text. In general, these errors are correlated. The second is the systematic error, which was taken to be the rms deviation of the central values of the appropriate fits in Table IX.

Figure 25. Resonance model fit to the data, excluding the one-star resonances and using a cutoff, $d = 0.10$. It is not significantly different from the best fit curves obtained for the seven other fits described in the text. The dashed line shows the best fit possible if the Δ (2200) is excluded.

Because there was no significant difference in either the goodness of fit or the character of the best fit curves for the two models it is clear that fits to the energy dependence of π^+p backward elastic scattering alone cannot determine which model more accurately represents physical reality. In any case, fits based on both models support the existence of a negative parity resonance at ~ 2200 MeV. Additional evidence for the existence of a $\Delta(2200)$ was obtained by substituting the best fit parameters into equations (1) to (6), using only the non-signatured part of (5), and predicting a slope parameter for each of the incident pion momenta. The structure observed in Figure 17 between 2.0 and 2.5 GeV/c could be reproduced only when the $\Delta(2200)$ was included.

CHAPTER V

CONCLUSION

The data obtained in this experiment were used to systematically study the energy dependence of $d\sigma/d\Omega$ at 180° in π^+p elastic scattering for incident pion momenta ranging from 2 to 6 GeV/c. Angular distributions were measured near 180° , and values for $d\sigma/d\Omega$ at 180° were obtained by fitting the distributions to the form $a \exp[b(u-u_{\max})]$. Fits to the backward cross sections were made using both a pure resonance model and an interference model. Both models led to equally good fits to the data and predicted values for the masses, widths, parities, and the product of spin and elasticity for the $\Delta(2200)$, $\Delta(2420)$, $\Delta(2850)$, and $\Delta(3230)$ resonances. On the basis of backward scattering alone it was not possible to determine which model more accurately describes pion-nucleon scattering. However, both models required the existence of the $\Delta(2200)$ in order to produce satisfactory fits to the data. Heretofore, the $\Delta(2200)$ has not been classified as a well-established resonance. This experiment has added to the already available evidence for its existence and has also contributed to our knowledge of the $\Delta(2420)$, $\Delta(2850)$, and $\Delta(3230)$ resonances.

APPENDIX I

ON-LINE COMPUTER PROGRAM

In addition to reading data and storing it on magnetic tape the on-line program, JUDY, was expected to perform certain tests and calculations which enabled the experimenter to easily monitor the experiment. A flow chart showing the overall plan devised to meet this objective is given in Figure 26. The program was written in FORTRAN IV but most of the subroutines, particularly those communicating with the peripheral devices were written in the Varian assembly language, DAS. The DAS subroutine, RLEC, which transferred the data from the interface to computer memory is given in its entirety in Figure 27.

The primary guideline used in writing JUDY was that during the 500 msec beam spill the program performed only those jobs which were directly related to reading in data and performing consistency checks. Lower priority jobs such as scope displays were performed between beam spills. A parameter, LOOP, was used to control the priority of a job. LOOP had values ranging from one to six and was reinitialized to one whenever a sense line indicated the presence of beam spill. This resulted in the program remaining in a tight loop taking data and making consistency tests during beam spill.

Between beam spills the value of LOOP was allowed to increase and the program executed lower priority jobs, the most important of

which was transferring the data to magnetic tape whenever the buffer was full. The mechanism for requesting the optional lower priority jobs involved entering two or three characters through the teletype to designate a specific job. This process was interrupted during spill time, but once it was completed a flag was set indicating that the job should be performed when LOOP reached the appropriate value. Most scope display and printing jobs initiated while LOOP was equal to four, five, or six were interrupted if they were not completed before the next spill. Thus, it was possible for a longer job to be interrupted several times before it was finally completed. This detail is not shown in the flowchart. On the other hand, some of the jobs performed when LOOP was four, five, or six involved the reading in more than two or three characters via the teletype and could easily require more than the 3.5 seconds between beam spills. These jobs precluded a frequent test for the presence of spill and the electronics were gated off while the computer performed them. In general, jobs in this category were requested at most once or twice during a run so as not to interfere with data taking.

Figure 26. Program JUDY flowchart.

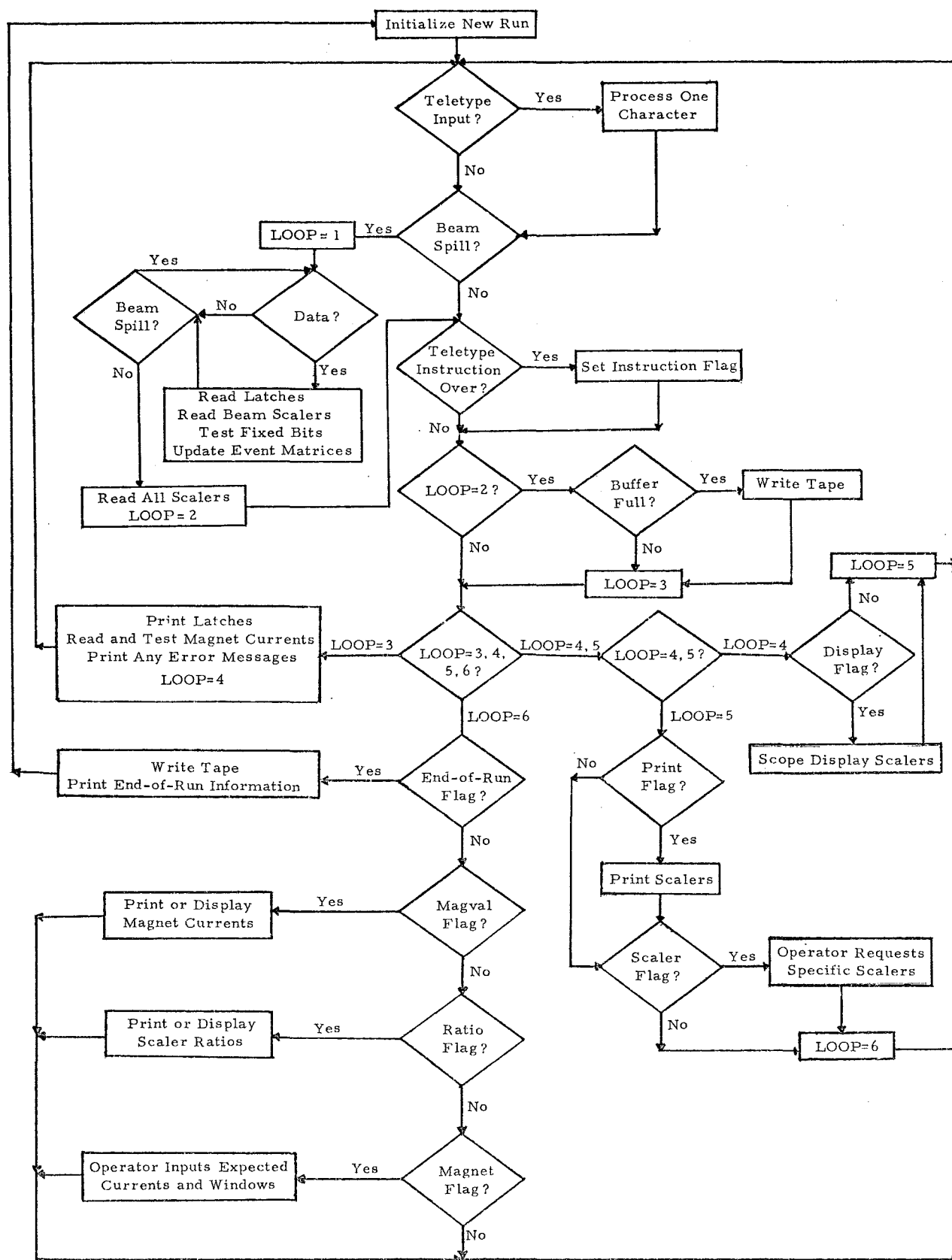


Figure 27. Listing of RLEC, the subroutine which transferred the data from the interface to computer memory. It is written in the Varian 620i assembly language, DAS.

```

*RLEC
*DAS SUBROUTINE RLEC(IBUF,N)
*READS N 24 BIT WORDS INTO MEMORY
*STORES THE FIRST WORD AT LOCATION IBUF
                                RLEC IS FORTRAN CALLABLE
000000 R ,FORT ,
000000 R ,NAME ,RLEC
000000 E CRLF ,EXT ,
000000 E PRIN ,EXT ,
000000 E $SE ,EXT ,
000000 000000 RLEC ,ENTR ,
000001 002000 ,CALL ,,$SE,2
000002 E
000003 000002
000004 000000 IBUF ,DATA ,0 $SE STORES IBUF HERE
000005 000000 N ,DATA ,0 $SE STORES N HERE
000006 006027 ,LDBE ,IBUF
000007 000004 R
000010 006017 ,LDAE* ,N
000011 100005 R
000012 054105 ,STA ,PAD
000013 005014 ,TAX ,
000014 006140 ,SUBI ,17 X=EXPECTED NO. OF WORDS
000015 000021
000016 001004 ,JAN ,SHRT GO DO SHORT READ
000017 000046 R
000020 100061 ,EXC ,061 START LONG READOUT
000021 014077 RL1 ,LDA ,THOU DELAY LOOP
000022 101061 RL2 ,SEN ,061,RL3 SENSE INTERFACE READY
000023 000031 R
000024 005311 ,DAR ,
000025 001010 ,JAZ ,EROR GO PRINT ERROR MESSAGE
000026 000054 R
000027 001000 ,JMP ,RL2
000030 000022 R
000031 064005 RL3 ,STB ,BLOC
000032 005122 ,IBR ,
000033 064001 ,STB ,ALOC
000034 102061 ,IME ,061,0 FIRST 16 BITS INTO MEMORY
000035 000000
000035 ALOC ,BES ,0 STORE LOW 16 BITS IN ALOC
000036 102061 ,IME ,061,0 NEXT 8 BITS INTO MEMORY
000037 000000
000037 BLOC ,BES ,0 STORE HIGH 8 BITS IN BLOC
000040 005122 ,IBR ,
000041 005344 ,DXR ,
000042 001040 ,JXZ ,RSET COUNT WORDS READ OUT
000043 000051 R
000044 001000 ,JMP ,RL1
000045 000021 R
000046 100261 SHRT ,EXC ,0261 START SHORT READOUT
000047 001000 ,JMP ,RL1
000050 000021 R
000051 100361 RSET ,EXC ,0361 DONE READING; RESET
000052 001000 ,JMP* ,RLEC RETURN FROM SUBROUTINE
000053 100000 R
000054 002000 EROR ,CALL ,PRIN PRINT ERROR MESSAGE
000055 000000 E
000056 000066 R L3 ,DATA ,THRE PRIN HAS 4 PARAMETERS
000057 000067 R LB ,DATA ,ERBF
000060 000070 R L4 ,DATA ,FOUR
000061 000071 R LZ ,DATA ,ZR
000062 002000 ,CALL ,CRLF CARRIAGE RETURN; LINE FEED
000063 000000 E
000064 001000 ,JMP ,RSET
000065 000051 R
000066 000003 THRE ,DATA ,03
000067 002635 ERBF ,DATA ,02635,04330
000070 004330
000071 000004 FOUR ,DATA ,04
000072 000000 ZR ,DATA ,0
000073 000000 PAD ,BSS ,01
000074 001750 THOU ,DATA ,1000
000000 ,END ,

```

APPENDIX II

CORRELATION MATRIX STUDIES

A sample of the matrices described in Section 3.2 is shown in Figure 28. This particular set shows the pairs of θ_2^B , θ_3^B and $\bar{D} \cdot \theta_4^B$ matrices for an incident pion momentum of 2.8 GeV/c. For an event to be included in a matrix on the left a particle had to be detected in the central ϕ_c^B counter. Events in which a particle was detected in either of the noncentral counters, ϕ_{nc}^{B1} and ϕ_{nc}^{B2} , are binned in the matrices on the right. Within a given matrix rows 1 through 8 correspond to P^F counters 1 through 8. Row 9 includes P^F counters 9 through 12. Row 10 gives the number of times there was no signal in any P^F counter and row 11 is the sum of rows 1 through 10. Columns 1 through 7 correspond to counters θ_1^F through θ_7^F . For $\bar{D} \cdot \theta_4^B$ the number of times no θ^F signal was detected is added to column 7. For θ_2^B and θ_3^B this number is added to column 1.

A comparison of the central and noncentral matrices for a given θ^B shows that they have similar θ^F dependences. However, the momentum dependences are not similar. This was indicated in Figure 12 and is even more obvious in Figure 29, which shows the momentum dependence in the beam-right and beam-left noncentral ϕ^B counters for each θ^B bin at 2.8 GeV/c. There is a clear correlation between the trajectory of backward pions which entered the noncentral ϕ^B counters and the distribution at the momentum hodoscope. This correlation

Figure 28. Hodoscope correlation matrices for an incident pion momentum of $2.8 \text{ GeV}/c$. The interpretation of the matrix elements is described in Section 3.2 and Appendix II.

$\theta_2^B \cdot (\text{CENTRAL } \phi^B \text{ COUNTER})$

4	6	-1	3	7	7	4	30
-3	2	6	5	27	39	2	78
34	4	-2	87	325	235	4	687
16	0	10	66	189	96	-1	376
2	2	1	8	16	12	1	42
2	1	0	3	4	2	0	12
2	1	0	4	6	6	1	20
0	1	0	0	1	2	0	4
1	0	0	2	1	2	0	6
1	3	6	25	66	53	2	156
59	20	20	203	642	454	13	1411

 $\theta_2^B \cdot (\text{NONCENTRAL } \phi^B \text{ COUNTERS})$

9	0	6	3	0	4	2	24
1	6	-2	13	24	11	0	53
8	2	4	9	27	13	2	65
4	3	2	3	3	2	0	17
-3	0	1	0	1	1	1	1
-2	0	1	-3	0	1	0	-3
1	0	1	1	6	1	0	10
1	0	0	0	0	0	0	1
0	0	0	0	0	1	0	1
6	4	2	7	13	4	2	38
25	15	15	33	74	38	7	207

 $\theta_3^B \cdot (\text{CENTRAL } \phi^B \text{ COUNTER})$

12	3	13	7	2	5	-3	39
6	6	12	18	9	-1	1	51
42	34	284	388	145	13	1	907
38	43	399	436	98	9	1	1024
2	6	64	61	24	0	0	157
3	-2	12	17	10	0	1	41
0	2	15	25	4	0	0	46
0	0	2	3	1	0	0	6
0	0	1	3	1	0	0	5
12	18	85	124	50	2	0	290
115	110	887	1082	344	28	1	2567

 $\theta_3^B \cdot (\text{NONCENTRAL } \phi^B \text{ COUNTERS})$

3	3	3	-2	1	1	0	9
9	3	29	23	18	3	0	85
5	10	29	50	6	1	0	101
4	4	19	8	8	1	0	44
0	4	17	8	2	1	-3	29
-2	0	13	8	1	0	0	20
1	0	8	9	4	0	0	22
0	0	5	3	1	0	0	9
-3	0	5	3	0	0	0	5
1	3	15	20	6	2	-3	44
18	27	143	130	47	9	-6	368

 $\bar{\theta}_4^B \cdot (\text{CENTRAL } \phi^B \text{ COUNTER})$

-7	0	11	3	-2	4	-6	3
-5	20	11	-1	5	2	3	35
25	304	406	49	2	1	37	824
26	440	468	69	-5	0	28	1026
2	81	82	5	0	1	10	181
1	19	26	4	0	1	0	51
2	24	22	4	1	0	2	55
2	4	6	0	0	0	0	12
0	5	4	-3	0	0	0	6
6	91	122	15	2	3	12	251
52	988	1158	145	3	12	86	2444

 $\bar{\theta}_4^B \cdot (\text{NONCENTRAL } \phi^B \text{ COUNTERS})$

6	6	3	4	2	4	-2	23
-2	19	17	2	5	4	3	48
3	30	20	2	3	0	2	60
-1	21	20	-5	2	2	1	40
0	20	15	2	1	0	3	41
-2	14	17	4	0	0	1	34
0	11	19	1	1	0	1	33
0	5	14	0	0	0	1	20
2	6	5	0	0	0	3	16
3	19	24	2	1	0	2	51
9	151	154	12	15	10	15	366

was observed at all values of incident pion momentum. Calculations done in the beam design program, TRANSPORT²², showed that the effect occurred because the low momentum components of the beam tended to be right divergent while the high momentum components tended to be left divergent.

The necessity for making the first correction described in Section 3.4 became apparent as a result of studying the areas under the dashed and solid curves for each θ^B counter in plots similar to the ones shown in Figure 29. In this figure the two areas are comparable for each of the $\mathcal{D}\cdot\theta_5^B$, $\mathcal{D}\cdot\theta_4^B$ and $\overline{\mathcal{D}}\cdot\theta_4^B$ bins. However, for θ_3^B the area under the solid curve is smaller than that under the dashed curve and for θ_2^B and θ_1^B it practically disappears. This phenomenon was understood as the result of a broken light pipe joint in the part of the ϕ_{nc}^{B1} counter shadowing θ_1^B , θ_2^B and part of θ_3^B . A similar break also produced an inefficiency in the part of ϕ_c^B shadowing these three counters. One estimate of the apparent inefficiencies in counters θ_1^B , θ_2^B , and θ_3^B caused by the inefficiency in ϕ_{nc}^{B1} was obtained by plotting the appropriately weighted number of events in each θ^B bin for the ϕ_{nc}^{B1} and ϕ_{nc}^{B2} counters separately. This is shown in Figure 30 for data taken at 2.8 GeV/c. Unfortunately this method could not be used for other incident pion momenta because of their poorer statistical accuracies. The method finally used to estimate the efficiencies involved plotting the angular distributions for each incident pion momentum. Two

Figure 29. Momentum dependence in the noncentral ϕ^B counters for the six θ^B bins at 2.8 GeV/c. The dashed curve represents the number of recoil protons whose backward pions entered the beam-right ϕ_{nc}^{B2} counter and the solid curve indicates the number of recoil protons whose backward pions entered the beam-left ϕ_{nc}^{B1} counter. The figure shows the data before the θ^F cuts and background subtraction were applied, but after the empty target subtraction had been made.

Figure 30. Angular distributions for the noncentral ϕ^B counters at 2.8 GeV/c. The crosses correspond to events whose backward pion entered the beam-right ϕ_{nc}^{B2} counter; the dots correspond to the beam-left ϕ_{nc}^{B1} counter. The points are data from the target-full runs, corrected only for geometric efficiency. The deviation of the dots from the straight line fit is interpreted as evidence for the inefficiency of the ϕ_{nc}^{B1} counter.

parallel lines were constructed, the upper line connecting the points in the $\mathcal{D} \cdot \theta_5^B$, $\mathcal{D} \cdot \theta_4^B$ and $\overline{\mathcal{D}} \cdot \theta_4^B$ bins and the lower line connecting the points in the θ_3^B , θ_2^B and θ_1^B bins. The difference between these two lines was a measure of the efficiencies of the latter counters. These efficiencies were plotted as a function of beam momentum. Correction factors used in the final determination of the differential cross sections were obtained from smooth curves fitted to these points. The slopes obtained using these correction factors agreed with slopes obtained from independent experiments^{2, 6, 15}.

APPENDIX III

PROPORTIONAL WIRE CHAMBERS

During the final stages of the analysis of the π^+p backward elastic scattering experiment the author participated in the preparations being made for two additional experiments. One phase of these preparations involved cleaning and running preliminary tests on proportional wire chambers that were designed and constructed at Notre Dame. The ground plane and the two high voltage planes in each chamber consisted of fine wires stretched across G-10 epoxy-glass frames. The technique used to clean these wire planes is described below:

1. Soak the plane for at least two minutes in a solution of Alconox glass cleaner and distilled water.
2. Rinse the plane in distilled water.
3. Soak the plane in absolute alcohol for at least six minutes.
4. Remove the plane from the alcohol and gently shake off the excess alcohol.
5. Place the plane on a dark surface and illuminate the wires using a good desk lamp. Leave one edge of the plane in contact with the surface and raise the other edge until it is possible to see the reflection of the light from the wires.
6. Gently wipe each wire using a Q-tip cotton swab which has been dipped in alcohol, paying particular attention to the wires having visible contamination.
7. Turn the plane over and repeat step 6.
8. When all three planes have been cleaned assemble the chamber, darken the room, and apply ~ 3500 V to the chamber. Increase the voltage in steps of 100 to 200 V and watch for corona on the wires. The chamber should be able to sustain ~ 5000 V before breakdown occurs.

9. If corona occurs for a potential difference less than 5000 V the chamber should be cleaned again with alcohol, giving special attention to the area where the discharge occurred. In most cases the contaminant will be found on a ground plane wire.
10. If the chamber passes the test described in step 8 it should be disassembled so that each plane can be soaked in alcohol again before it is finally reassembled. After reassembly no high voltage should be applied until the chamber has been sealed.

APPENDIX IV

BIBLIOGRAPHY

In the course of analyzing the data and writing this dissertation the author encountered a number of other works which are of interest relative to the general subject of backward πp elastic scattering, even though they were not directly relevant to this particular study. These articles are categorized and listed below. In those cases where several articles describe the same experiment only the most recent publication is listed. No attempt was made to obtain an exhaustive set of references for each of the categories.

- A. Differential cross sections for $\pi^+ p$ elastic scattering where u is less than -0.14 (GeV/c)² and/or the incident pion momentum is outside the range 2 to 6 GeV/c.

C. W. Akerlof, P. K. Caldwell, P. Kalbaci, D. I. Meyer, K.C. Stanfield, P. N. Kirk, A. Lesnik, D. R. Rust, C. E. W. Ward, and D. D. Yovanovitch, " $\pi^\pm p$ Elastic Scattering and $\pi^+ p \rightarrow K^+ \Sigma^+$ at 5.0 GeV/c Near $-t = 3.0$ (GeV/c)²," Physical Review Letters 27, 219 (1971).

H. H. Atkinson, C. R. Cox, P. J. Duke, K. S. Heard, D. P. Jones, A. R. Kemp, P. G. Murphy, J. D. Prentice, and J. J. Thresher, "Measurements of Differential Cross Sections and Polarization Effects in Pion-Proton Elastic Scattering in the Momentum Range 875 to 1579 MeV/c," Proceedings of the Royal Society A289, 449 (1966).

P. J. Bussey, J. R. Carter, D. R. Dance, D. V. Bugg, A. A. Carter, A. M. Smith, " πp Elastic Scattering from 88 to 292 MeV," Nuclear Physics B58, 363 (1973).

V. Chabaud, A. Eide, P. Lehman, A. Lundby, S. Mukhin, J. Myrheim, C. Baglin, P. Briandet, P. Fleury, M. Davier, V. Gracco, R. Morand, D. Treille, "Measurement of Large-Angle $\pi^\pm p$ Elastic Scattering at 5 GeV/c," Physics Letters 38B, 441 (1972).

J. A. Helland, T. J. Devlin, D. E. Hagge, M. J. Longo, M. J. Moyer, and C. D. Wood, "Elastic Scattering of Positive Pions by Protons in the Energy Range 500-1600 MeV," *Physical Review* 134B, 1062 (1964).

P. M. Ogden, D. E. Hagge, J. A. Helland, M. Banner, J. F. Detoeuf, and J. Teiger, " π -p Elastic Scattering in the Energy Range 300-700 MeV," *Physical Review* 137B, 1115 (1965).

J. Orear, R. Rubinstein, D. B. Scarl, D. H. White, A. D. Krisch, W. R. Frisken, A. L. Reed, and H. Ruderman, "Pion-Proton Elastic Scattering at High Momentum Transfers," *Physical Review Letters* 15, 309 (1965).

M. L. Perl, L. W. Jones, and C. C. Ting, "Pion-Proton Elastic Scattering from 3 GeV/c to 5 GeV/c," *Physical Review* 132, 1252 (1963).

D. R. Rust, P. N. Kirk, R. A. Lundy, C. E. W. Ward, D. D. Yovanovitch, S. M. Pruss, C. W. Akerlof, K. S. Han, D. I. Meyer, and P. Schmueser, "Structure in 5-GeV/c π^+ p Elastic Scattering at Large Angles," *Physical Review Letters* 24, 1361 (1970).

J. Va'vra, " π^+ p Backward Elastic Scattering Between 1.25 and 3.0 GeV/c," Thesis, McGill University, 1972 (unpublished).

B. Polarization data for π^+ p Backward Elastic Scattering.

M. G. Albrow, S. Andersson/Almehed, B. Bošnjaković, C. Daum, F. C. Erne, J. P. Lagnaux, J. C. Sens, and F. Udo, "Elastic Scattering of Positive Pions on Polarized Protons between 0.82 and 2.74 GeV/c," *Nuclear Physics* B25, 9 (1970).

F. Bradamante, S. Conetti, C. Daum, G. Fidecaro, M. Fidecaro, M. Giorgi, G. Kalmus, A. Penzo, L. Piemontese, P. Schiavon, D. Stairs, and A. Vascotto, "Polarization in Backward π^+ p Scattering at 2.0, 3.5, and 4.0 GeV/c," *Nuclear Physics* B56, 356 (1973).

L. Dick, Z. Janout, H. Aoi, C. Caverzasio, A. Gonidec, K. Kuroda, A. Michalowicz, M. Poulet, D. Sillou, D. G. Aschman, N. E. Booth, K. Green, and C. M. Spencer, "Measurement of the Polarization Parameter in π^+ p Backward Elastic Scattering at 6 GeV/c," *Nuclear Physics* B43, 522 (1972).

D. J. Sherden, N. E. Booth, G. Conforto, R. J. Esterling, J. Parry, J. Scheid, A. Yokosawa, "Measurement of the Polarization in Backward Angle π^+ p Elastic Scattering between 2.50 and 3.75 GeV/c," *Physical*

Review Letters 25, 898 (1970).

C. Backward Elastic π^- p Scattering Data.

E. W. Anderson, E. J. Bleser, H. R. Blieden, G. B. Collins, D. Garelick, J. Menes, F. Turkot, D. Birnbaum, R. M. Edelstein, N. C. Hien, T. J. McMahon, J. Mucci, and J. Russ, " π^- p Elastic Scattering Near 180° at 8 and 16 GeV/c," Physical Review Letters 20, 1529 (1968).

A. Brabson, G. Calvelli, S. Cittolin, P. DeGuio, F. Gasparini, S. Limentani, P. Mittner, M. Posocco, L. Ventura, C. Voci, M. Crozon, A. Diaczek, R. Sidwell, and J. Tocqueville, "Backward π^- p Elastic Scattering at 3 and 4 GeV/c," Physics Letters 42B, 283 (1972).

S. W. Kormanyos, A. D. Krisch, J. R. O'Fallon, K. Ruddick, and L. G. Ratner, "Structure in π^- p Elastic Scattering at 180° ," Physical Review Letters 16, 709 (1966).

E. S. Meanley, R. W. Anthony, C. T. Coffin, J. E. Rice, N. R. Stanton, and K. M. Terwilliger, " π^- p Elastic Scattering near 180° from 2.15 to 6 GeV/c," Physical Review D6, 740 (1972).

R. J. Ott, J. Trischuk, J. Va'vra, T. J. Richards, and L. S. Schroeder, " π^- p Backward Elastic Scattering between 1.28 and 3.0 GeV/c," Physics Letters 42B, 133 (1972).

M. Perl, Y. Y. Lee, and E. Marquit, "Large Angle π^- p Elastic Scattering at 3.63 GeV/c," Physical Review 138B, 707 (1965).

D. Total cross section data showing evidence for the existence of the Δ (2420), Δ (2850), and Δ (3230).

A. Citron, W. Galbraith, T. F. Kycia, B. A. Leontic, R. H. Phillips, A. Rousset, and P. H. Sharp, "Structure in the Pion-Proton Total Cross Section between 2 and 7 GeV/c," Physical Review 144, 1101 (1966).

A. N. Diddens, E. W. Jenkins, T. F. Kycia, and K. F. Riley, "Structure in the Pion-Proton Total Cross Section between 2 and 3 BeV," Physical Review Letters 10, 262 (1963).

REFERENCES

1. Aachen-Berlin-Birmingham-Bonn-Hamburg-London (I.C.) - Munchen Collaboration, "Elastic π^+p Scattering at 4 GeV/c," Physics Letters 10, 248 (1964).
2. W. F. Baker, P. J. Carlson, V. Chabaud, A. Lundby, J. Banaigs, J. Berger, C. Bonnel, J. Duflo, L. Goldzahl, and F. Plouin, "Elastic Backward Scattering of Pions and Kaons," Nuclear Physics B9, 249 (1969).
3. W. F. Baker, K. Berkelman, P. J. Carlson, G. P. Fisher, P. Fleury, D. Hartill, R. Kalbach, A. Lundby, S. Mukhin, R. Nierhaus, K. P. Pretzl, and J. Woulds, "Elastic Forward and Backward Scattering of π^- and K- mesons at 5.2 and 7.0 GeV/c," Nuclear Physics B25, 385 (1971).
4. H. Brody, R. Lanza, R. Marshall, J. Niederer, W. Selove, M. Shochet, and R. Van Berg, "Measurement of $\pi^\pm p$ Backward Scattering at 4 to 8 GeV/c," Physical Review Letters 18, 828 (1966).
5. W. Busza, B. G. Duff, D. A. Garbutt, F. F. Heymann, C. C. Nimmon, K. M. Potter, T. P. Swetman, E. H. Bellamy, T. F. Buckley, R. W. Dobinson, P. V. March, J. A. Strong, and R. N. F. Walker, " $\pi^\pm p$ Elastic Scattering in the 2-GeV Region," Physical Review 180, 1339 (1969).
6. A. S. Carroll, J. Fischer, A. Lundby, R. H. Phillips, C. L. Wang, F. Lobkowicz, A. C. Melissinos, Y. Nagashima, and S. Tewksbury, " $\pi^\pm p$ Backward Scattering Between 1.5 and 3.0 BeV/c," Physical Review Letters 20, 609 (1968).
7. C. T. Coffin, N. Dikmen, L. Ettlinger, D. Meyer, A. Saulys, K. Terwilliger, and D. Williams, "Elastic Differential Cross Sections for $\pi^\pm p$ Scattering from 2.3 - 6.0 BeV/c," Physical Review 159, 1169 (1967).
8. V. Cook, B. Cork, W. Holley, and M. L. Perl, "Elastic Differential Cross Section of π^+p at 1.5, 2.0, and 2.5 BeV/c," Physical Review 130, 762 (1963).
9. D. E. Damouth, L. W. Jones, and M. L. Perl, "Pion-Proton Elastic Scattering at 2.00 GeV/c," Physical Review Letters 11, 287 (1963).

10. L. Dick, Z. Janout, H. Aoi, C. Caverzasio, A. Gonidec, K. Kuroda, A. Michalowicz, M. Poulet, D. Sillou, D. G. Aschman, N. E. Booth, K. Green, and C. M. Spencer, "Measurement of the Polarization Parameter in π^+p Backward Elastic Scattering at 6 GeV/c," Nuclear Physics B43, 522 (1972).
11. T. Dobrowolski, B. N. Gus'kov, M. F. Likhachev, A. L. Lubimov, Yu. A. Matulenko, V. S. Stavinsky, and A. S. Vovenko, "Structure in π^+p Elastic Backward Scattering," Physics Letters 24B, 203 (1967).
12. W. R. Frisken, A. L. Read, H. Ruderman, A. D. Krisch, J. Orear, R. Rubinstein, D. B. Scarl, and D. H. White, "Backward Elastic Scattering of High-Energy Pions by Protons," Physical Review Letters 15, 313 (1965).
13. F. E. James, J. A. Johnson, and H. L. Kraybill, "Elastic Differential Cross Sections for π^+p at 1.76 and 2.08 GeV/c," Physics Letters 19, 72 (1965).
14. J. MacNaughton, W. R. Butler, D. G. Coyne, G. M. Hicks, and G. H. Trilling, " π^+p Elastic Scattering at 3.6 GeV/c," Nuclear Physics B33, 101 (1971).
15. D. P. Owen, F. C. Peterson, J. Orear, A. L. Read, D. G. Ryan, D. H. White, A. Ashmore, C. J. S. Damerell, W. R. Frisken, and R. Rubinstein, "High-Energy Elastic Scattering of π^\pm , K- and \bar{p} on Hydrogen at c.m. Angles from 22° to 180° ," Physical Review 181, 1794 (1969).
16. D. J. Schotanus, C. L. Pols, D. Z. Toet, R. T. Van de Walle, J. V. Major, G. E. Pearson, B. Chaurand, R. Vanderhaghen, G. Rinaudo, and A. E. Werbrouck, "Study of Cross Sections and Spin-Density Matrix Elements for Two-Body Reactions in 5 GeV/c π^+p Two-Pronged Interactions," Nuclear Physics B22, 45 (1970).
17. R. A. Sidwell, R. R. Crittenden, K. F. Galloway, R. M. Heinz, and H. A. Neal, "Backward π^+p Elastic Scattering from 2.18 to 5.25 GeV/c," Physical Review D3, 1523 (1971).
18. A. S. Vovenko, B. N. Gus'kov, M. F. Likhachev, A. L. Lyubimov, Yu. A. Matulenko, I. A. Savin, and V. S. Stavinskii, "Elastic 180° Scattering of π^+ Mesons by Protons at High Energies," JETP Letters 2, 255 (1965).

19. S. S. Yamamoto and D. C. Rahm, "Two-Prong Interaction by π^+ p Collisions at 2.77 BeV/c," *Physical Review* 173, 1302 (1968).
20. A summary of the experimental situation as of January, 1968 is given by Malcolm Derrick in Backward Peaks (Experimental), ANL/HEP 6802, Argonne National Laboratory, Argonne, Illinois.
21. A compilation of π^+ p differential cross section measurements listed according to incident pion momentum is included in π N Two-Body Scattering Data, part I. LBL-63, by the Particle Data Group, Lawrence Berkeley Laboratory, Berkeley, California (April, 1973).
22. K. L. Brown and S. K. Howry, "TRANSPORT/360, A Computer Program for Designing Charged Particle Beam Transport Systems," SLAC-91, available from Clearinghouse for Federal Scientific and Technical Information, Springfield, Virginia, (July, 1970).
23. D. C. Carey, "TURTLE, A Computer Program for Simulating Charged Particle Beam Transport Systems," NAL-64, December, 1971 (unpublished).
24. W. F. Baker, D. P. Eartly, K. P. Pretzl, S. M. Pruss, A. A. Wehmann, P. Koehler, A. J. Lennox, J. A. Poirier, C. A. Rey, and O. R. Sander, "Energy Dependence of Backward π^+ p Elastic Scattering from 2 to 6 GeV/c," *Physical Review Letters* 32, 251 (1974).
25. C. A. Rey, A. J. Lennox, J. Poirier, and K. P. Pretzl, "New Parameters for the Δ^{++} Resonances from 2170 to 3490 MeV in π^+ p Backward Elastic Scattering," *Physical Review Letters* 32, 908 (1974) and 33, 250 (1974).
26. R. E. Rothschild, T. Bowen, P. K. Caldwell, D. Davidson, E. W. Jenkins, R. M. Kalbach, D. V. Petersen, and A. E. Pifer, " π^\pm - Proton Elastic Scattering at 180° from 0.60 to 1.60 GeV/c," *Physical Review* D5, 499 (1972).
27. C. B. Chiu and A. V. Stirling, "Validity of the Interference Model for π N Scattering?," *Physics Letters* 26B, 236 (1968).
28. R. Dolen, D. Horn, and C. Schmid, "Finite-Energy Sum Rules and Their Application to π N Charge Exchange," *Physical Review* 166, 1768 (1968).

29. E. Ma and G. L. Shaw, "Duality in $\pi^+ p$ Elastic Scattering," Physical Review D3, 1264 (1971).
30. V. Singh, "Regge Poles in πN Scattering and in $\pi + \pi \rightarrow N + N$," Physical Review 129, 1889 (1963).
31. V. Barger and D. Cline, "Fermion Regge-Pole Model for the Structure of Pion-Nucleon Elastic Scattering in the Backward Hemisphere," Physical Review 155, 1792 (1967).
32. E. Ma and G. L. Shaw, "Duality in πN Scattering," (unpublished).
33. Other investigators have suggested the existence of a negative parity Δ resonance having mass $\sim 2200 \text{ MeV}/c^2$. See references [6], [29], [34], [36] - [39].
34. P. G. Tomlinson, R. A. Sidwell, D. B. Lichtenberg, R. M. Heinz, and R. R. Crittenden, "Duality and the Comparison of Resonance and Regge Models for $\pi^+ p$ Backward Scattering," Nuclear Physics B25, 443 (1971).
35. This amount was calculated using the approximation that the quantity $\sqrt{2\chi^2} - \sqrt{2n_D}$ has unit standard deviation, where n_D is the number of degrees of freedom. See R. A. Fisher, Statistical Methods for Research Workers (Edinburgh, London, 1938).
36. W. von Schlippe, "Evidence for a G_{39} - Resonance in πN Scattering," Lettere al Nuovo Cimento 4, 767 (1972).
37. J. L. Rosner, "Spectroscopic Consequences of Exact Duality for Baryons," Physical Review D7, 172 (1973).
38. F. Wagner, "A Phase Shift Analysis for πN Using a Regge Model," presented at the XVI International Conference on High Energy Physics at the University of Chicago and Fermi National Accelerator Laboratory, (Sept., 1972).
39. R. Shanta, "Backward π -p Elastic Scattering in the Momentum Range 1.0 to 5.5 GeV/c," Il Nuovo Cimento 70, 12 (1970).